CONTENTS

Annual Subscription

Pakistan: Rs 250
Foreign Countries: US$ 40
Overseas Air Mail Charges: US$ 10

The Journal is published bi-annually
In April and October

Published by:
Riaz Ahmad for Government College University, Lahore, Pakistan.

Printed at:
PRIME Publishers.

JOURNAL OF NATURAL SCIENCES AND MATHEMATICS

INFORMATION FOR AUTHORS

1. TYPES OF PAPERS ACCEPTED

The Journal aims at publishing original research papers and the review papers from stinguished scientists on Mathematics, Physics, Chemistry and Computer Science.

2. SUBMISSION OF MANUSCRIPTS

Manuscripts should be submitted in MS Word format through e-mail to the relevant editor. ll papers are refereed. The decision of the Editorial Board regarding the acceptance and ublication of the paper will be final.

3. PREPARATION OF MANUSCRIPT

1 Language and Style

All submissions should be in English; typed in double spacing on one side of the paper only with a left hand margin of at least 4 cm. Mathematical expressions must be carefully printed. Computer composed manuscript on C.D. or through e-mail in MS Word format is required for speedy publication.

2 Abstract

This should comprise a brief and factual summary of contents and should be suitable for rect use by abstracting journals. This will seldom require more than 200 words.

3 Section/Sub-Section Headings

Papers should be divided into sections / sub-sections and numbered as exemplified in e headings of this INFORMATION FOR AUTHORS.

4 References

References should be numbered consecutively in the text, e.g. "According to a recent eory [6]...it is well established [7]" and collected at the end of the paper in following style:

6. I. M. Ghauri and P. Feltham, J. Nat. Sci. Math., 26 (1986) 63.
7. W. Greiner and J. Maruhn, Nuclear Models, Springer-Verlag, Berlin, (1996).

5 Illustrations

Line diagrams must be drawn in black ink on white paper; original and two copies are quired. Photographs or half-tone reproduction should be in the form of highly glazed prints. gures are also acceptable in the form of jpg or tif format of 300 dpi. A separate list of captions r illustrations should be provided.

4. PROOFS

Only one set of proof is sent to the authors for correction.

PK ISSN 0022- 2941; CODEN JNSMAC
Vol. 54, (2014) PP 01-10

EVALUATION OF NUCLEAR REACTION CROSS SECTIONS FOR THE PRODUCTION OF AN EMERGING DIAGNOSTIC RADIONUCLIDE ^{120}I VIA PROTON INDUCED REACTIONS ON ^{120}TE AND ^{122}TE

L. A. KHAN[1], N. AMJED[1,2], M. HUSSAIN*[1]

[1]Department of Physics, Government College University Lahore, Pakistan.

[2]School of Allied Health Science, The Children's Hospital and Institute of Child Health, Lahore, Pakistan.

*E-mail address: dr.mazharhussain@gcu.edu.pk

(Received: 22-09-2014)

ABSTRACT: Excitation functions for the production of ^{120}I is measured via ^{120}Te(p,n)^{120}I and ^{122}Te(p,3n)^{120}I nuclear reactions up to 35 MeV and 45 MeV respectively, using stacked foil technique. Initially the experimental data were scrutinized for consistency; thereby some experimental data sets were normalized for their discrepancies of monitor and decay data. Excitation functions compared with theoretical nuclear model calculations of ALICE-IPPE and TENDL-2013. Nuclear reactions were found to be interesting for medical applications and particularly first reaction is important for the production of ^{120}I at small sized cyclotrons. Production of radionuclide is useful especially in tumour imaging as well as in some cardiac and cerebral studies using Positron Emission Tomography.

Keywords: Excitation function, tumour imaging.

1. INTRODUCTION

The nuclear reaction data accessed from different sites is not extensive; only literature overview data is compiled for concerning evaluation. Discrepant data from the whole process will be rejected but some is selected for evaluation. Mostly, the data of low energy is e.g. 30 MeV needed for applications but for certain radionuclide's production of higher energy data (e.g. 80 MeV) is required [1]. Quality of data is available on major sources of database EXFOR, from data center at Vienna [1]. Prepared files from EXFOR included complete information's and compilation of proton induced reaction's data. In current work, data for proton-induced and deuteron induced reactions for the production of ^{120}I will be evaluated.

Radionuclide ^{120}I ($T_{1/2}$=1.35h) is unstable isotope, obtained via EC-process to ^{120}Te (i.e. naturally occurring) [2]. The radioisotope ^{120}I is suitable short lived β+ emitter which has emerging importance in life sciences [2]. Positron emitters having long half-lives are significant, used to study slow metabolic processes and quantification processes etc [1]. Because of hurdles in positron emitter's, exact calculations of isomeric cross sections, extensive experiments (low transition energies) are needed to define levels of isomeric impurities [3]. IAEA-NDC (Nuclear data centres) are struggling to discover more suitable radionuclides for health care purposes and to develop new positron emitter radionuclides because of the growth in utilization in medical fields [3]; ^{120}I is one of them.

Analysis of nuclear reaction cross sections of emerging radionuclide ^{120}I ($T_{1/2}$=1.35 h) requires to examine its suitability in medical applications. It can be produced both in reactors and at cyclotrons via many nuclear reactions. But through cyclotron have more advantages to get more tense (radioactive) data, demanded for medical investigations [3]. In this work we have investigated its production cross sections via proton induced reactions on ^{120}Te and ^{122}Te, they have natural abundance 0.09% and 2.55% respectively. Production yield of ^{120}I through ^{120}Te(d,x)^{120m,g}I reaction channel is very low, make it unsuitable for medical applications, Hohn et al. [4]. Production through natural tellurium is not suitable due to excess of impurities.

The ^{124}Xe (p, n+α)^{120}I reaction doesn't have practical importance, excluded from investigations. Because of low target composition i.e 0.09532, it will be low yield calculation, much hard to enrich ^{124}Xe for production of ^{120}I, Hermanne et al. [6]. The radioisotope originally produced via ^{127}I(p,8n)Xe^{120}→[EC,40 min]^{120g}I reaction with 340 MeV incident energy is hard to achieve, Hohn et al. [5].

2. EVALUATION METHODOLOGY

Data evaluation procedure requires combination of experimental data with theoretical models to get best values of cross sections [1]. Data evaluation methodology is to ensure the quality of the data in life sciences. Purpose of methodology is to develop ENDF file for medical specialty [1]. The Evaluation methodology is involves the compilation of all experimental data including full description from i.e. EXFOR and performs examination of reliability of the data [7]. Then perform adjustment of data according to detectors efficiency, γ-ray intensity, flux monitoring, etc. Then make sure the Consistency from different laboratories. Then we use computer code ALICE-IPPE and theoretical results of TENDL-2013 to execute nuclear model calculations. Then perform comparison of experimental data values with theoretical results for standardization of data and also perform impurities analysis produced in different energy regions during reaction. The details of the evaluation methodology have already been reported by us.

3. EVALUATION OF (p,n) REACTION

Data available on database is not extensive for this reaction, two sets are selected of Guray et al. [8] and Hohn et al. [9] reported for 120g'ml. Guray et al. [8] used activation method i.e. γ-ray spectrometry up to 7.93 MeV and Tandem Van de Graaff accelerator is used, experiment performed at Argonne National Laboratory, Argonne, IL,USA. While, Hohn et al. [9] executed results with stacked irradiation techniques up to 35.2 MeV, through cyclotron, experiment performed at Forschungszentrum Juelich, Germany. Guray et al. [8] is suitable; no dissimilarities recovered comparing with NUDAT-2.6. Highly enriched target is used. In Guray et al. [8], beam current monitors via Faraday Cup, Hohn et al. [9] which used natCu(p,xn)62,63Zn and natTi(p,x)48V reactions. In pre-equilibrium region ALICE-IPPE calculations are moving towards higher energies but TALYS calculations are suited well in this region. Compound region is missing both theoretical results which are reported at higher cross. Optical region is matches well for both calculations.

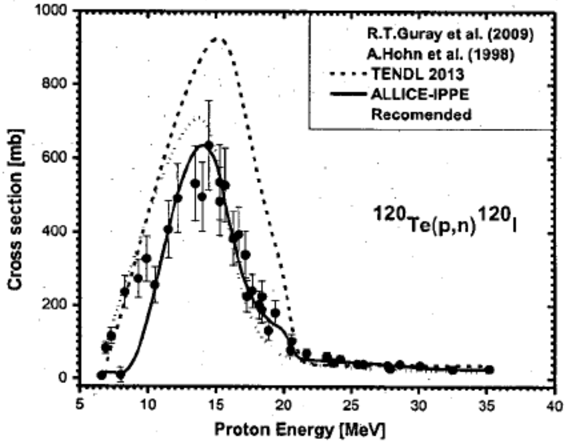

Fig. 1: Excitation functions for ^{120}Te(p,n)^{120}I reaction process and comparison with values of ALICE-IPPE and TENDL-2013.

Nuclear model calculations, ALICE-IPPE and TALYS calculations employed on dominated impurity ^{119}I by ^{120}Te(p,2n)^{119}I reaction to get experimental results. The production of ^{119}I during this reaction is 4.4%, Hohn. et al. [9]. The activities examined at 257.5 keV (86.7%) of γ-rays. Beyond 28 MeV just ^{119}I is observed along with ^{120g}I, while errors inspected for ^{119}I in cross section is 17%, Hohn et al. [9]. Short half-life of ^{119}I(19.1 min), pertain no serious problems for ^{120g}I production for application purposes, Hohn et al. [9].

Table 1: Recommended cross sections of proton induced nuclear reaction on ^{120}Te.

Energy(MeV)	Cross-section(mb)	Energy(MeV)	Cross-section
	$^{120}Te(p,n)^{120}I$		$^{120}Te(p,n)^{120}I$
6.5	19 ± 2	21	56 ± 4
7	18 ± 1	21.5	53 ± 4
7.5	18 ± 1	22	51 ± 4
8	14 ± 1	22.5	50 ± 4
8.5	22 ± 2	23	49 ± 4
9	51 ± 4	23.5	48 ± 4
9.5	98 ± 8	24	47 ± 4
10	167 ± 13	24.5	46 ± 4
10.5	243 ± 19	25	46 ± 4
11	327 ± 26	25.5	44 ± 4
11.5	407 ± 33	26	43 ± 3
12	482 ± 39	26.5	42 ± 3
12.5	541 ± 43	27	41 ± 3
13	590 ± 47	27.5	40 ± 3
13.5	621 ± 50	28	38 ± 3
14	642 ± 51	28.5	37 ± 3
14.5	624 ± 50	29	35 ± 3
15	599 ± 48	29.5	34 ± 3
15.5	515 ± 41	30	32 ± 3
16	427 ± 34	30.5	31 ± 2
16.5	350 ± 28	31	30 ± 2
17	278 ± 22	31.5	29 ± 2
17.5	235 ± 19	32	28 ± 2
18	196 ± 16	32.5	28 ± 2
18.5	176 ± 14	33	27 ± 2
19	157 ± 13	33.5	27 ± 2
19.5	146 ± 12	34	27 ± 2
20	133 ± 11	34.5	27 ± 2
20.5	98 ± 8	35	28 ± 2

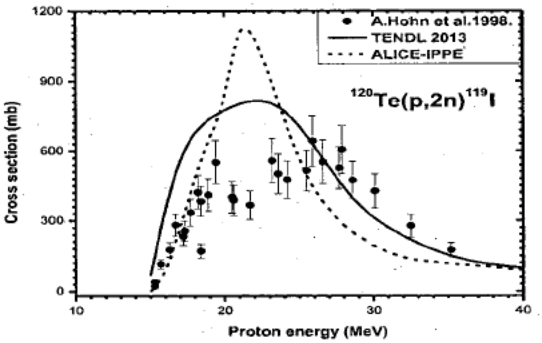

Fig. 2: Excitation functions for $^{120}Te(p,2n)^{119}I$ reaction process and comparison with values of with values of ALICE-IPPE and TENDL-2013.

Quantity produced for ^{120g}I with pure target is 2.3 GBq/μAh which is sufficient in optimum energy range which is 15-9 MeV, Hohn et al. [9]. Experimentally calculated yield is 7.1 GBq/μAh Hohn et al. [5]. In current reaction contribution of ^{120m}I is <10% during the production of ^{120g}I Hohn et al. [5].

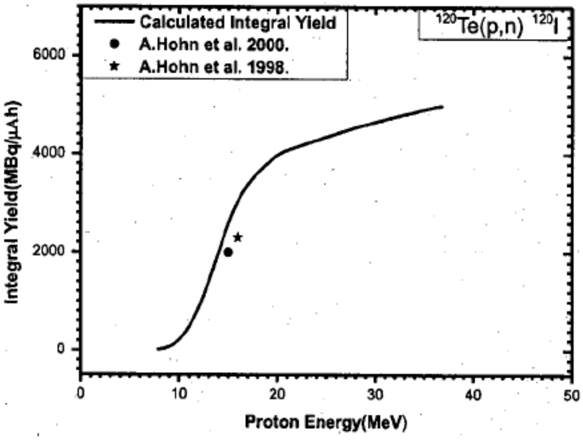

Fig. 3: Calculated integral yield of ^{120}I as a function of proton energy by $^{120}Te(p,n)^{120}I$ reaction and comparison with experimental results.

The main drawback in particular reaction is higher cost of enriched ^{120}Te(0.09%) as compared to ^{122}Te(2.55%), Hohn et al, [5]. The curve in Figure 3 shows the calculated yield ^{120}I for our work. The Optimum energy range where the yield of ^{120}I is higher and impurities are minimum is 16→11 MeV, as impurities are calculated by Hohn et al, [5] in this energy range.

Table 2: Calculated thick target yields for the production of ^{120}I during $^{120}Te(p,n)$ reaction.

Target Thickness energy range(MeV)	Yield of ^{120}I (MBq/μAh)(mCi/μAh)
16→11	1939 (52)
20→17	3795(102)
28→21	4363(118)
39→29	4818(130)

4. EVALUATION OF (p,3n) REACTION

Experimental data available for (p, 3n) reaction is consists of 2 set at both ground and isomeric states Hohn et al. [5]. Excitation functions evaluated up to 45 MeV via stacked-foil techniques. Highly enriched ^{122}Te is used, with isotopic composition 97.12, while natural composition is 2.55%. Beam currents monitor reactions used in Hohn et al. [5] was $^{nat}Cu(p,xn)^{62,63}Zn$ and $^{nat}Ti(p,x)^{48}V$. By comparing these monitor's cross sections with TECDOC-1211 [1], no significant disagreement perceived. Actual error in cross section's examination is detected, 5-15%, Hohn et al. [5]. Gamma-ray intensity, while comparison with NUDAT-2.6 is not considerable differences observed.

In pre-equilibrium region ALICE-IPPE calculations have good agreement with experimental results, but TALYS calculations are present at low energies. Compound region is missing both calculations but lying in same energy region. In optical region TALYS calculations are matching well with experimental results but ALICE calculations are moving towards low energy.

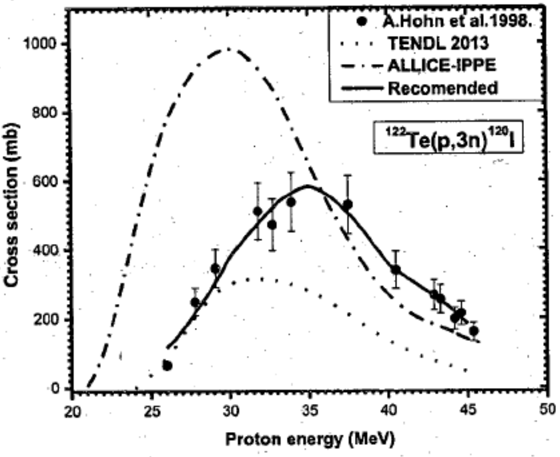

Fig. 4: Excitation functions for ^{122}Te(p,3n)^{120}I reaction process and comparison with theoretical code and literature values.

Investigations of (p,3n) reaction shows that beta-emitted from ^{120g}I at end point energy, which may cause disturbance due to presence of ^{120m}I, Hohn et al. [5]. Cross sections within 32-37 MeV i.e. peak regions are slightly uncertain due to preliminary nature, Hohn et al. [5]. Level of all impurities remains constant except ^{119}I which causes no problem due to short half-life (19.1 min), Hohn et al. [5].

Nuclear model calculation employed for standardizing cross sections of ^{122}I during ^{122}Te(p,3n)^{122}I reaction, shown in Fig. 5. Cross-section error calculated for ^{119}I is 17%, same as that of $^{120m+g}$I, [9]. The concentration of impurity ^{119}I in range (37-32 MeV) is 6%, but throughout reaction production rate is varying and increases adjacent with energy, Hohn et al. [9].

Table 3: Cross sections of proton induced nuclear reaction on ^{122}Te.

Energy(MeV)	Cross-section(mb)	Energy(MeV)	Cross-section(mb)
	^{122}Te(p,3n)^{120}I		^{122}Te(p,3n)^{120}I
26	116 ±9	36	563 ±45
26.5	138 ±11	36.5	549 ±44
27	166 ±13	37	526 ±42
27.5	196 ±16	37.5	504 ±40
28	232 ±19	38	480 ±38
28.5	262 ±21	38.5	450 ±36
29	298 ±24	39	417 ±33
29.5	336 ±27	39.5	390 ±31
30	379 ±30	40	355 ±28
30.5	406 ±32	40.5	339 ±27
31	434 ±35	41	322 ±26
31.5	459 ±37	41.5	307 ±25
32	485 ±39	42	291 ±23
32.5	511 ±41	42.5	278 ±22
33	536 ±43	43	262 ±21
33.5	552 ±44	43.5	245 ±20
34	565 ±45	44	228 ±18
34.5	578 ±46	44.5	205 ±16
35	586 ±47	45	184 ±15
35.5	576±46		

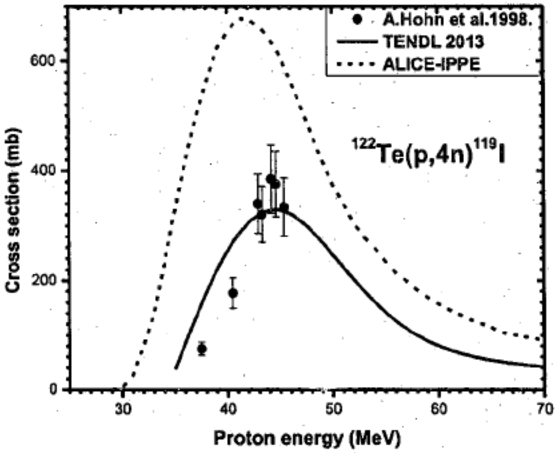

Fig. 5: Excitation functions for ^{122}Te(p,4n)^{119}I reaction process and comparison with ALICE-IPPE and TENDL-2013.

Error in cross sections is amounted 14%; however concentration of impurity would be 22% for ^{121}I, Hohn et al. [5]. Impurity level of ^{121}I, approximately remains constant throughout reaction, Hohn et al. [5].

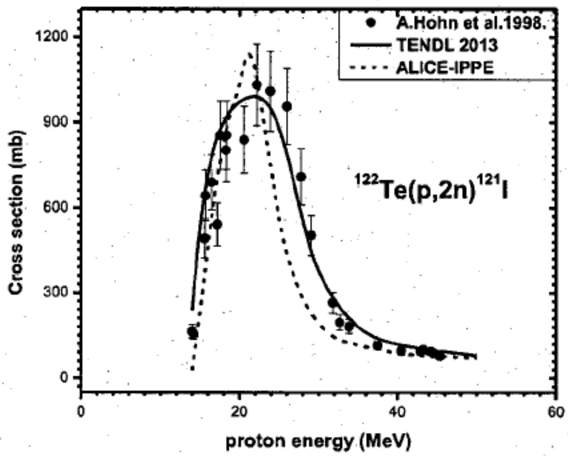

Fig. 6: Excitation functions for ^{122}Te (p,2n)^{121}I reaction process and comparison with theoretical code and literature values.

Best region for the production of ^{120g}I is compound region in between 30-40 MeV with yield 3.6 GBq/μAh, Hohn et al.[9]. Whereas impurities production rate for this reaction was calculated as ^{120m}I (25%), ^{121}I(22%) and ^{119}I(6%), Hohn et al.[5].

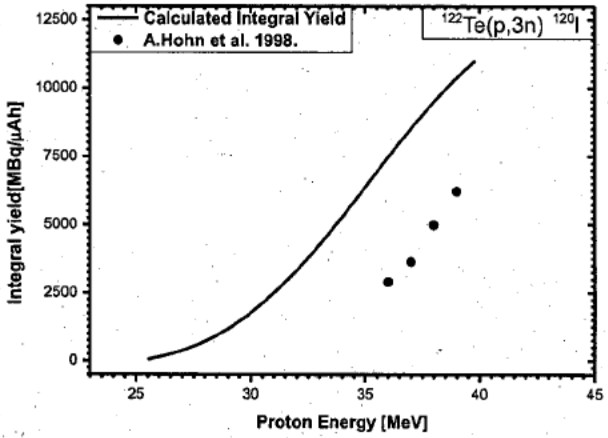

Fig. 7: Calculated integral yield of ^{120}I as a function of proton energy by ^{122}Te(p,3n)^{120}I reaction and comparison with experimental results.

Optimum energy range for the production of ^{120}I during this reaction is 37→32 MeV as selected by, Hohn et al. [9]. The calculated yield in this energy range 3624

MBq/μAh (98 mCi/μAh) which is sufficient for medical applications. Another region for the production of ^{120}I (31→29 MeV) is weak, and impurities are dominated in this region.

Table 4: Calculated thick target yields for the production of ^{120}I during ^{122}Te(p,3n) reaction.

Target Thickness energy range(MeV)	Yield of ^{120}I (MBq/μAh)(mCi/μAh)
31→29	2163(58)
37→32	3624(98)

5. CONCLUSIONS

The proton induced reactions on ^{120}Te and ^{122}Te were evaluated using stacked foil techniques. The measured cross sections were compared with calculations of ALICE-IPPE and TENDL 2013. After some adjustments, calculated and measured excitation functions have good agreement for proton induced reactions. The recommended data should be useful for optimization of various routs for the production of ^{120}I.

REFERENCES

1. K. Gul, A. Hermanne, M. G. Mustafa, F. M. Nortier, S. M. Qaim, B. Scholten, Yu. Shubin, S. Takacs, F. Tarkanyi and Y. Zhuang, Charged Particle Cross Section Database for Medical Radioisotopes Production: Diagnostic Radioisotopes and Monitor Reactions; IAEA-TECDOC-1211, (2001) 285.
2. A. Hohn, H. H. Coenen and S. M. Qaim, Radiochim. Acta, 88 (2000) 139.
3. S. M. Qaim, Radiochim Acta, 100 (2012) 635.
4. A. Hohn, H. H. Coenen and S. M. Qaim, Appl. Radiat. Isot., 52 (2000) 923.
5. A. Hohn, B. Scholten, H. H. Coenen and S. M. Qaim, Appl. Radiat. Isot., 49 (1998) 93.
6. A. Hermanne, F. Tarkanyi, S. Takacs, R. Adam, A. Ignatyuk, S. Spellerberg and R.Schweikert, Appl. Radiat. Isot., 69 (2) (2011) 358.
7. http://www-nds.iaea.org/exfor/exfor.htm
8. R. T. Guray, N. Ozkan, C. Yalcm, A. Palumbo, R. deBoer, J. Gorres, P. J. Leblanc, S. O'Brien, E. Strandberg, W. P. Tan, M. Wiesher, Z. Fulop, E. Somoraji, H. Y. Lee and J. P. Greene, Physical Review C, 80 (3) (2009) 035804.
9. A. Hohn, H. H. Coenen and S. M. Qaim, Appl. Radiat. Isot., 49 (1998) 1493.
10. A. Hohn, H. H. Coenen and S. M. Qaim, Appl. Radiat. Isot., 52 (2000) 923.

11. S. M. Qaim, A. Hohn, Th. Bastian, K.M. El-Azoney, G. Blssing, S. Spellerberg, B. Scholten and H. H. Coenen, Appl. Radiat. Isot., 58 (2003) 69.

12. A. M. Ahmed, H. E. Hassan, K.F.Hassan, A. M. Khalaf and Z. A. Saleh, Radiochim. Acta, 99 (2011) 323.

13. K. M. El-Azony, K. Suzuki, T. Fukumuraa, F. Szelecsenyi and Z. Kovacs, Radiochim. Acta, 96 (2008) 769.

14. A. J. Koning, D. Rochman, S. C. Marck, J. Kopecky, J. Ch. Sublet, S. Pomp, H. Sjostrand, R. Forrest, E. Bauge, H. Henriksson, O. Cabellos, S. Goriely, J. Leppanen, H. Leeb, A. Plompen and R. Mills , New and advance version of TALYS 1.4 TENDL (2013).

15. http://www.nndc.bnl.gov/nudat2.6/

16. S. Sudar, A. Hohn and S. M. Qaim, Appl. Radiat. Isot., 52 (2000) 941.

PK ISSN 0022- 2941; CODEN JNSMAC
Vol. 54, (2014) PP 11-26

DEPOSITION OF TITANIUM DIOXIDE (TiO_2) THIN FILMS ON Si (100) USING PULSED DC GLOW DISCHARGE

M. S. ABBAS*[1], R. AHMAD[1], T. HUSSAIN[1], U. IKHLAQ[2], S. SALEEM[2] AND M. S. ANJUM[2]
[1]Center for Advanced Studies in Physics (CASP), Government College University Lahore, Pakistan.
[2]Department of Physics, Government College University Lahore, Pakistan.

.*E-mail address: msabbas424@gmail.com

(Received: November 11, 2013)

ABSTRACT: TiO_2 thin films are deposited on silicon (100) and glass substrate by 100 Hz pulsed dc glow discharge in the mixed Ar and O_2 plasma using Titanium metal as sputtering target. The effects of both filling pressure and operating power on film structure, chemical composition and surface morphology are studied. The film structure and chemical composition is characterized by X-ray diffraction (XRD) and Fourier Transform Infrared Spectroscopy (FTIR). The surface morphology is investigated by Scanning electron microscopy (SEM) and Atomic Force Microscope (AFM). The XRD results suggest that the TiO_2 thin film deposited on both the substrates is amorphous in nature because there is no extra peak found in the XRD results which may be related to any form of titanium dioxide (TiO_2) whereas the FTIR results confirm the presence of titanium dioxide thin film with vibrational modes in the wavenumber range from 700-1000 cm^{-1}. SEM results depict that sputtering increases with power resulting in the increased formation of TiO_2 on silicon substrate. Ionized oxygen also oxidizes the substrate and form bubble like structure as visible on the SEM micrographs. The surface morphology of the deposited titanium dioxide thin films at varying filling pressure shows spherical, bubble like and flower like structure. AFM results show that all the samples depict almost rough surface composed of closely packed titanium dioxide particles of various grain sizes and root mean square roughness values ranging from 2 nm to 8 nm showing combination of rough and uniform thin films.

Keywords: O_2 plasma, Pulsed dc, Fourier Transform Infrared Spectroscopy, Surface roughness, Vibrational mode, Wavenumber.

1. INTRODUCTION

There is increasing interest in commercial production of titanium dioxide (TiO_2) because it is widely being used as a pigment in paints, in sunscreen as UV absorber and as a photocatalyst under UV light. Titanium dioxide has three crystalline phase rutile, anatase and brookite. Each of these has superior electrical, structural, thermal and optical properties because of which it has surpassed many other materials in the market. Even the amorphous titanium dioxide, because of its high refractive index and corrosion resistance, has many optical applications. For the first time in 1972, Fujishima and Honda [1] discovered the photocatalytic property of titanium dioxide. They found water splitting in hydrogen and oxygen by titanium dioxide under UV irradiation. Since then, there have been tremendous efforts employed on the research of TiO_2 material. Due to these efforts, number of promising applications has aroused ranging from photovoltaics and antireflective coating to oxygen sensors.

Various techniques such as CVD, MOCVD, PECVD, PLD, spray pyrolysis, sol-gel and sputter deposition have been adopted to deposit titanium dioxide thin films on various substrates depending upon the application.

2. EXPERIMENTAL SETUP

The glow discharge was created by Pulsed DC sputtering system which consists of vacuum chamber, electrode assembly, vacuum generation system and pulsed DC power supply.

The vacuum chamber is the AISI 304 stainless steel made cylinder of 45 cm internal diameter and 45 cm height. The vacuum chamber has two removable stainless steel plates of diameter 30 cm. The twice of the plates have electrodes attached at the centre of the plates and mounted inside the chamber. The upper plate of the chamber lifts open to allow the access to the substrate and the target. At the top of the chamber there are three NW-16 ports, two of them are used for the inlet of the gases while on third, a capsule type dial vacuum gauge is attached for the pressure measurement. The circular side of the chamber has 5 multipurpose ports covered with stainless steel plates. One of them is covered with Quartz plate which serves as view window and with one of these ports an OES spectrometer can be attached for recording the OES data as shown in the figure 1.

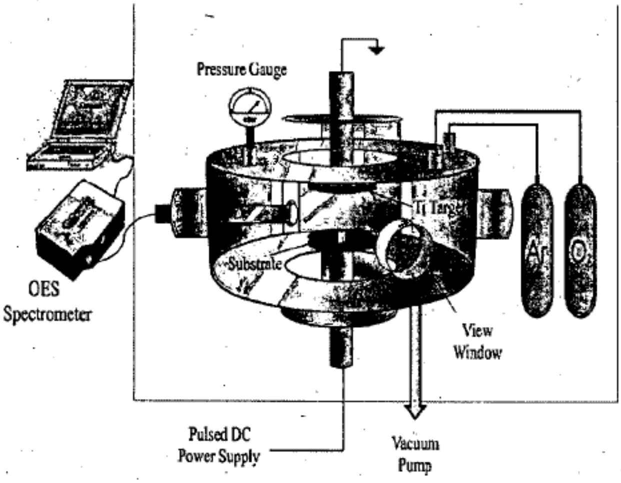

Fig. 1: Pulsed dc glow discharge experimental setup.

Two electrodes pierced through upper and lower plates from the center are mounted inside the chamber in parallel plate configuration. The lower electrode is the 42 mm diameter electrode made up of stainless steel attached to the positive terminal of the power supply which serves as anode. The substrates glass and silicon wafers are placed on this electrode just at the center. The upper grounded electrode is made up of pure titanium metal which serves as sputtering target. The purity of the titanium metal used as target was checked by XRD pattern as shown in the figure 2.

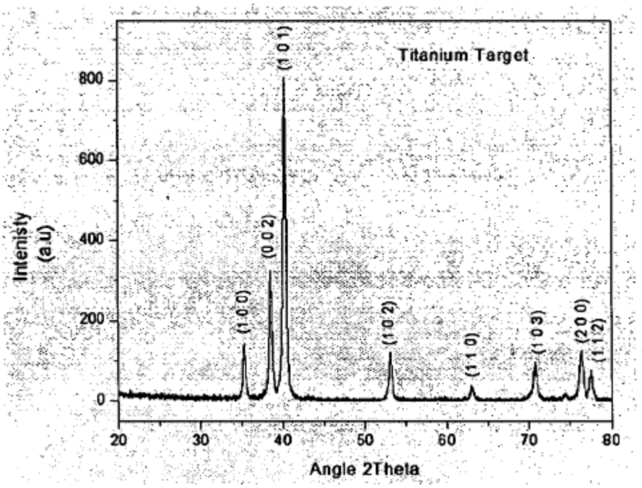

Fig. 2: XRD Pattern of Titanium target.

The inter electrode distance is such that it can be varied according to the requirement by moving upper electrode outside. The electrodes are covered with ceramic cups so that the discharge should remain within the central area of electrodes also the steel rods connected with electrodes are sealed by ceramic rods. From the lower end of the chamber, a rotary pump is used to create vacuum inside the chamber. A capsule type gauge is attached with the system to measure the internal pressure of the chamber

There is availability of various process parameters to study the properties and structure of titanium dioxide thin films prepared by reactive pulsed dc sputtering. In this experiment, the sputtering power and overall filling gas pressure of the chamber were focused. The pulsed dc power was varied from 180 W to 240 W with fixed optimum pressure of 1 mbar. The Overall filling gas pressure was varied from 0.5 mbar to 2 mbar with fixed Power of 220 W. All the deposition parameters are summarized in Table 1.

Argon to oxygen ratio was taken as 80/20 and was controlled by the needle value of the capsule type gauge. Further increase in oxygen partial pressure oxidizes the sputtering target and forms an oxide layer on the target which hinders the sputtering process. Also the target was pre-sputtered in pure argon plasma to remove impurities on the target surface. Optimized inter-electrode distance and working time was taken 3cm and 4hrs respectively.

Table 1: Summary of process parameters used during experiment.

Parameter	Range	Status
Pulsed DC power	180-240 Watt	Varied
Chamber pressure	0.5 mbar – 2.0 mbar	Varied
Gas Composition	20 % O_2 + 80 % Ar	Fixed
Inter-electrode distance	3 cm	Fixed
Deposition time	4 hrs/ sample	Fixed
Substrate type	Silicon, glass	Varied

Silicon and glass samples were used as substrate. The silicon samples were cut from the silicon wafer in 2cm×2cm dimension whereas the glass samples were cut from glass slides made of soda lime glass in the 2cm×2cm dimension. All Si samples were cleaned by acetone and were dried.

3. RESULTS AND DISCUSSION

3.1 Structural Characterization of the deposited TiO_2 thin film

Structural characterization of resultant thin film was studied by PANalytical X'Pert MRD X-ray diffractometer with Cu K-α radiation ($\lambda = 1.5406$Å) operated at a voltage of 40kV and a current of 40 mA in (θ-θ) scan mode. All the samples were scanned in the 2θ range between 20° and 80° with scan step of 0.03°.

Fig. 3 shows the X-ray diffraction patterns of TiO_2 thin films prepared on Si substrate for various pulsed DC power with fixed inter-electrode distance at 3cm and fixed filling pressure of 1 mbar. The diffractogram of untreated silicon shows intense peak of Si [100] at 2θ angle of 69°. For the treated sample at 180W power the diffractogram shows no extra peak in the pattern and the intensity of the original peak at 69° decreases. On further increasing the power, similar pattern is formed and the peak at 69° goes on decreasing thus no extra peak indicates that the thin film formed is amorphous in nature [1]. The last spectrographs d and e in the above figure are shown as straight lines but in fact these have small bumps at 69° with increased FWHM.

The reduction in the peak intensity at 69° by increasing the power indicates the significant increase in the deposition of the TiO_2 thin film. This is because with the increase of power, the sputtering rate increases. Since TiO_2 film is amorphous, peak intensity decreases and peak also broadens as discussed by other authors [1].

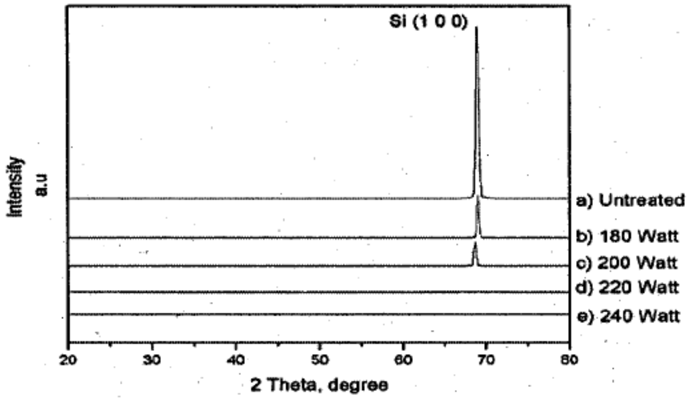

Fig. 3: XRD patterns of TiO_2 thin film deposited on Si (100) with variation in pulsed dc power.

Fig. 4 is the XRD pattern for the TiO_2 thin film deposited on glass substrate with same deposition conditions which suggests that the thin film formed is amorphous in nature as no well defined peaks related to titanium dioxide are detected.

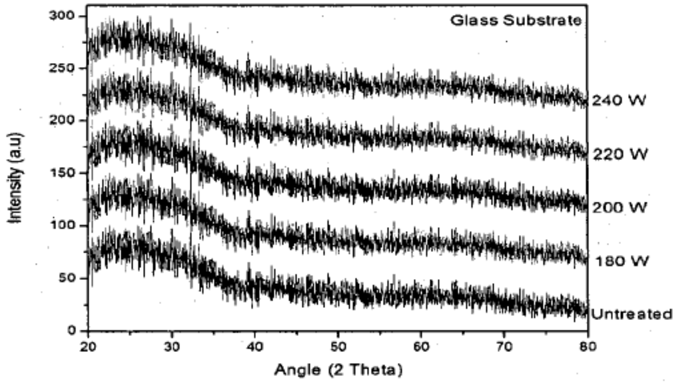

Fig. 4: XRD Pattern for the TiO_2 thin film deposited on glass substrate with variation in pulsed DC power

Fig. 5 shows the XRD pattern for the thin films prepared on silicon substrate at varying filling pressure with fixed power and inter-electrode distance. The spectrograms show small bumps at 2theta angle of 69°. By increasing the chamber pressure from 0.5 mbar to 2 mbar there is no big difference seen in the XRD pattern. There is no extra peak found in the XRD pattern which indicates the formation of amorphous titanium dioxide thin film.

X-ray diffraction analysis suggests that there are no well defined peaks found which can be related to any form of titanium dioxide thus thin film deposited on Si substrate is amorphous in nature because of the reason that the islands of titanium dioxide were amorphous [2]. Thin films deposited on glass substrate are also amorphous because of the different lattice mismatch of titanium dioxide phases on amorphous glass substrate [2].

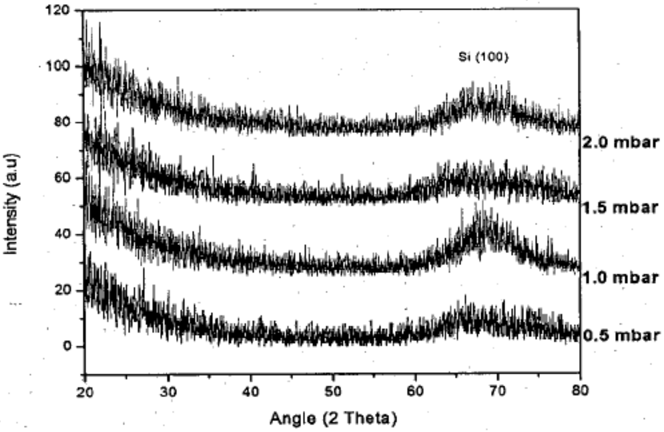

Fig. 5: XRD pattern for TiO_2 thin film deposited on Si (100) with variation in filling pressure

This may also be due to the fact that different kinds of substrate have different mobility of atoms on the substrate surface which is responsible for the degree and type of nucleation on the substrate [3].

3.2 Chemical Characterization of TiO_2 thin film by FTIR Spectroscopy.

The bond configuration and chemical composition of deposited Titanium dioxide thin film on Si substrates was investigated by ThermoFisher Scientific Nicolet 6700 FTIR Spectrometer in the ATR mode for spectral range from 650-4000 cm^{-1}. The FTIR Spectra for treated Si wafer with variation in power is shown in the following figure 6.

The FTIR spectra for the TiO_2 film prepared at 180 W, 200 W, 220 W and 240 W have different bands. A band is observed in the wavenumber range of 700 to 1000 cm^{-1} which corresponds to the formation of Ti-O and Ti-O-Ti bonds [4, 5, 6]. The peak at 739 cm^{-1} is attributed to the amorphous nature of TiO_2 thin film [5, 7]. The band in the wavenumber range of 1000 to 1200 cm^{-1} corresponds to the formation of Si–O–Si, Si–C and Si–O–C bonds [8, 9, 10]. The peak at 1430 cm^{-1}, 1720 cm^{-1} and 2360 cm^{-1} arises due to C = C, C = O and O = C = O bonds [11]. All these bands with corresponding wavenumber are summarized in table 2.

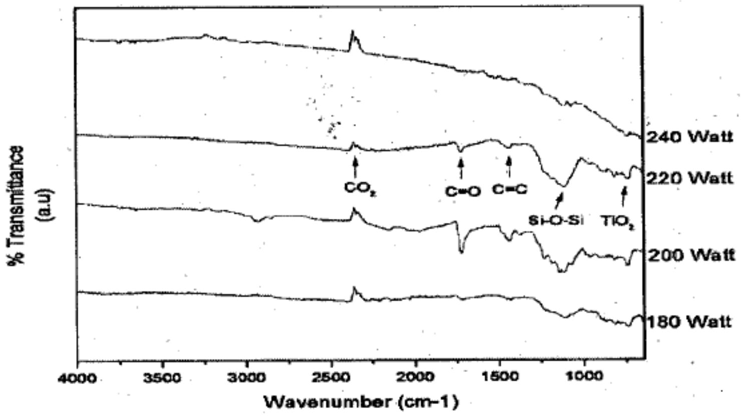

Fig. 6: FTIR Spectra for the TiO_2 thin film prepared on Si with variation in pulsed DC Power.

Table 2: IR frequencies and band assignment for the TiO_2 thin films deposited on Si wafer for varying pulsed dc power and filling pressure.

Wavenumber (cm^{-1})	**Band Assignment**
700-1000	Ti – O, Ti – O –Ti
739	TiO_2
1000-1200	Si – O – Si, Si – O – C,
1430	C = C
1720	C = O
2360	CO_2

The peak at 739 cm^{-1} is attributed to the formation of amorphous form of TiO_2. The broader peak at 1110 cm^{-1} corresponds to the formation of SiO_2 which indicates that the oxidation of substrate has also happened. Some carbonaceous contamination has also appeared at 1430 cm^{-1} and 1720 cm^{-1}. This carbon contamination has appeared due to already present carbon in the silicon wafers during the manufacturing process [9]. Small peak at 2360 is attributed to CO_2 which arises due to the cavity formed between the sample surface and IR source as contamination during analysis. By increasing the power, similar kind of spectra is formed. There is an increase in the intensity of Si – O – Si bond which indicates the increase of oxidation of Si substrate.

Similar kind of spectra is recorded for the TiO_2 thin film deposited on Si (100) for the variation of filling pressure as shown in the fig. 7. The peak for Si – O – Si bond almost diminishes at lower pressure. As the pressure is increased there is no significant change seen in the FTIR Spectra. At pressure 2 mbar a small peak appears near 3450 cm^{-1} which is attributed to the hydroxyl group [10]. Si – OH may have been formed due to moisture onto the deposited thin film.

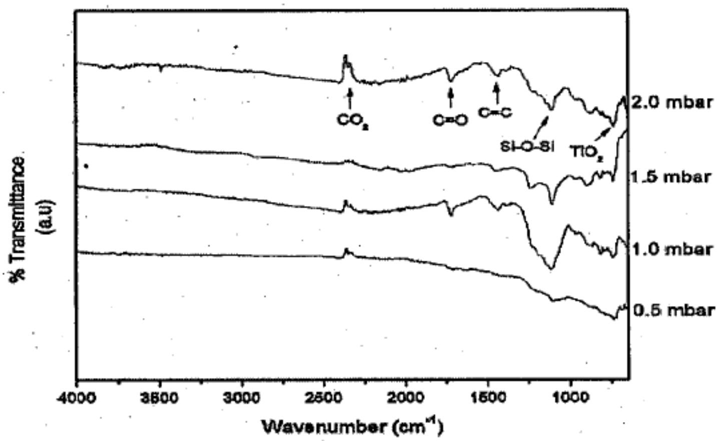

Fig. 7: FTIR spectra for the TiO_2 thin film deposited on Si (100) with variation in filling pressure.

3.3 Surface Morphology of TiO_2 thin film using SEM

The surface morphology of the pulsed dc sputtered TiO_2 thin films on silicon was observed using JEOL JSM-6480 LV Scanning Electron microscope.

Fig. 8 (a) shows the SEM micrograph of virgin sample of silicon wafer at 10 μm with magnification of (× 2,500). The surface is very clean and clear from any contamination. The thin film prepared at pulsed dc power of 180 W with fixed filling pressure of 1mbar reveals titanium dioxide particles scattered and splashed onto the entire surface of silicon as shown in the Fig. 8 (b). With increasing the power, the particles start to agglomerate and form flower like structure as shown in the Fig. 8 (c).

At power 220 W there is a mixture of small titanium dioxide particles and bigger particles which may be due to the oxidation of silicon surface. The oxide particles of silicon form bullet like structure as shown in the Fig. 8 (d). On further increasing the power a rough and dense thin film with diffused and merged titanium dioxide particles are formed as shown in the Fig. 8 (e). This depicts that sputtering increases with power resulting in the increased formation of TiO_2 on silicon substrate. Ionized oxygen also oxidizes the substrate and form bubble like structure as visible on the SEM micrographs.

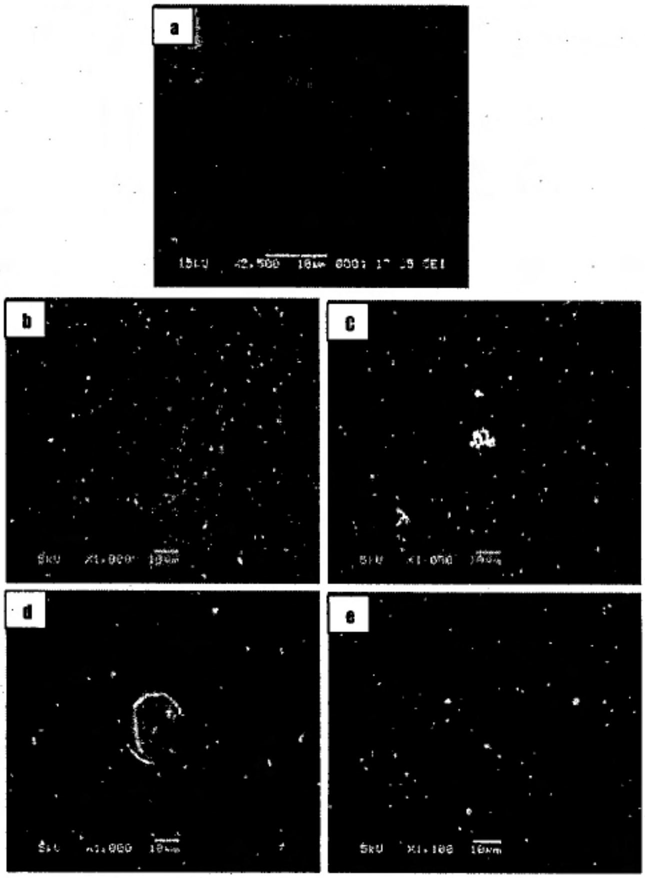

Fig. 8: SEM micrographs for TiO_2 thin film at various pulsed DC Power a) Untreated b)180 Watt c) 200 Watt, d) 220 Watt e) 240 Watt

Fig. 9 shows the effect of variation of filling pressure on the structure of titanium dioxide thin film. Fig. 9 (a) depicts titanium dioxide thin film prepared at low pressure of 0.5 mbar. This image has spherical particles splashed and scattered on silicon surface. At 1mbar pressure there is a circular structure formed having bubble like particles spread around in circular fashion with titanium dioxide particles. At 1.5 mbar and 2 mbar there are small amount of titanium dioxide particles formed as compared to the low pressure treated samples which may be due to the fact that by increasing the filling pressure the oxygen partial pressure increases which oxidizes the titanium target and an oxide layer on the target material is formed which results in the reduction of sputtering [12]. This reduction in sputtering decreases the deposition rate and reduces the growth of thin film as shown in the Fig. 9 (c) and (d).

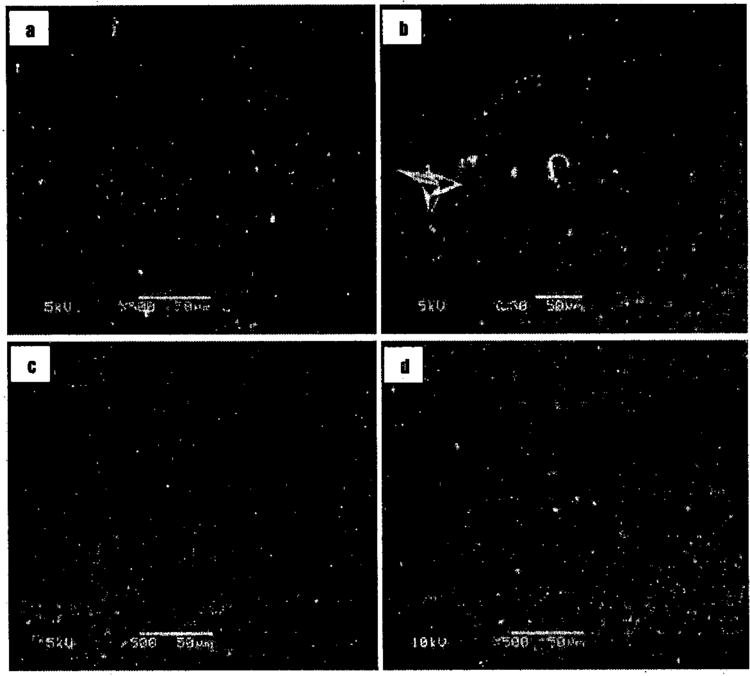

Fig. 9: SEM micrographs for TiO_2 thin film at various filling pressure a) 0.5 mbar b) 1 mbar c) 1.5 mbar d) 2 mbar.

The result obtained from SEM analysis suggests that there is a significant influence of power on the structure and growth of thin film. The variation in applied power increases sputtering yield and in result of that deposition increases, whereas the filling pressure in the chamber do have impact on the structure and thin film growth. By increasing the oxygen partial pressure there is reduction in the deposition rate [2], which is due to the fact that at higher filling pressures the oxygen partial pressure inside the chamber increases which poisons the titanium target and reduce the sputtering because metallic titanium is more sensitive to ionic bombardment than oxides as also observed by various authors [12,13].

3.4 Surface Topography of TiO_2 thin film using AFM

The surface topography and roughness of titanium dioxide thin film was investigated by Atomic Force Microscope SPM 9500 J. The unexposed sample of silicon wafer has clear surface as shown in the following figure 10. There are few bright spots which are due to some impurity items on the surface.

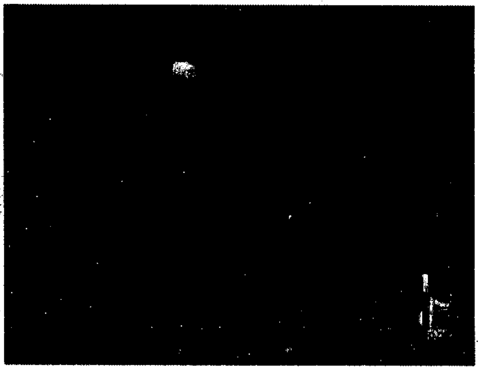

Fig. 10: AFM image for untreated silicon.

Fig. 12 represents the typical AFM images for the sample prepared at various pulsed DC powers. Left images represent the surface morphology and right images are typical three dimensional representations of the titanium dioxide thin film for the scale 5 µm × 5 µm. All the samples depict almost rough surface composed of closely packed titanium dioxide particles of various sizes. The treated samples at low power of 180 W and 200 W have smaller particles as shown in the fig. 11 (a & b). On further increasing the power, more dense film is formed having rough surface texture consisted of particles fused together at the inter particle connect building high mountains and deep valleys [14]. The films are composed of network of spherical nodules as it is clear from the fig. 11 (c & d). There is a considerable influence on the growth of film with the increase in power which is the strong correlation with the SEM Analysis.

The measured R_{rms} of the thin films prepared as a function of power is depicted in fig. 11. The higher roughness values represent the less homogeneity of the deposited thin film whereas the lower roughness values confirm the good homogeneity of the deposited thin films. At higher power of 240 watt the deposited thin film have less roughness which is related to the good homogeneity.

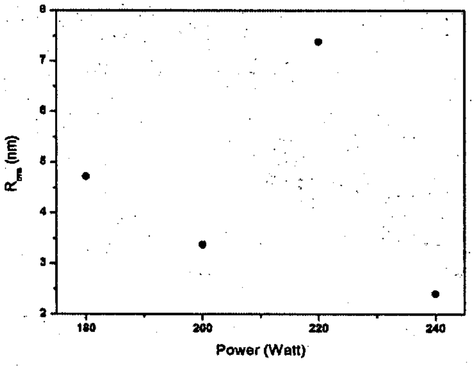

Fig. 11: R_{rms} of the TiO_2 thin films prepared at varying power.

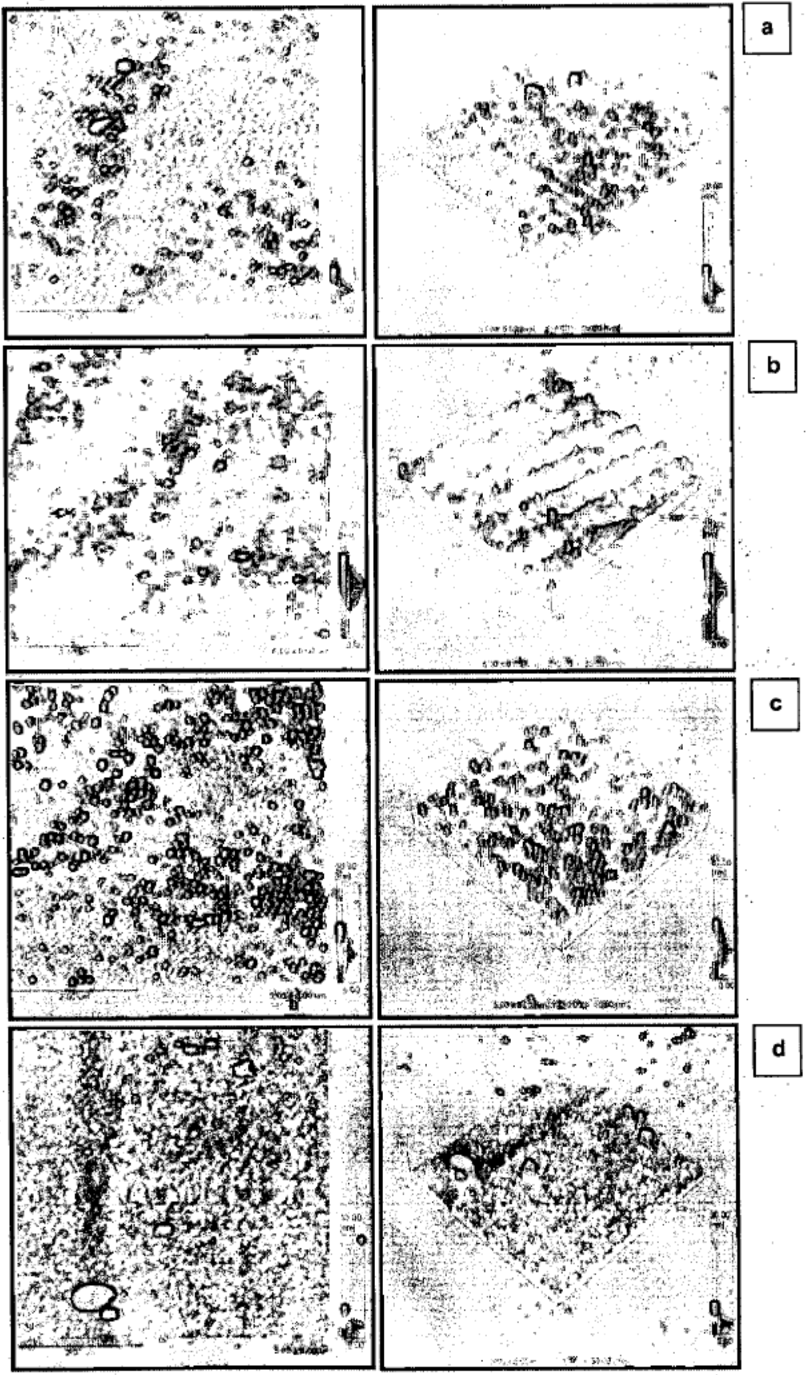

Fig. 12: AFM images for varying pulsed dc power a) 180 W b) 200 W c) 220 W d) 240 W

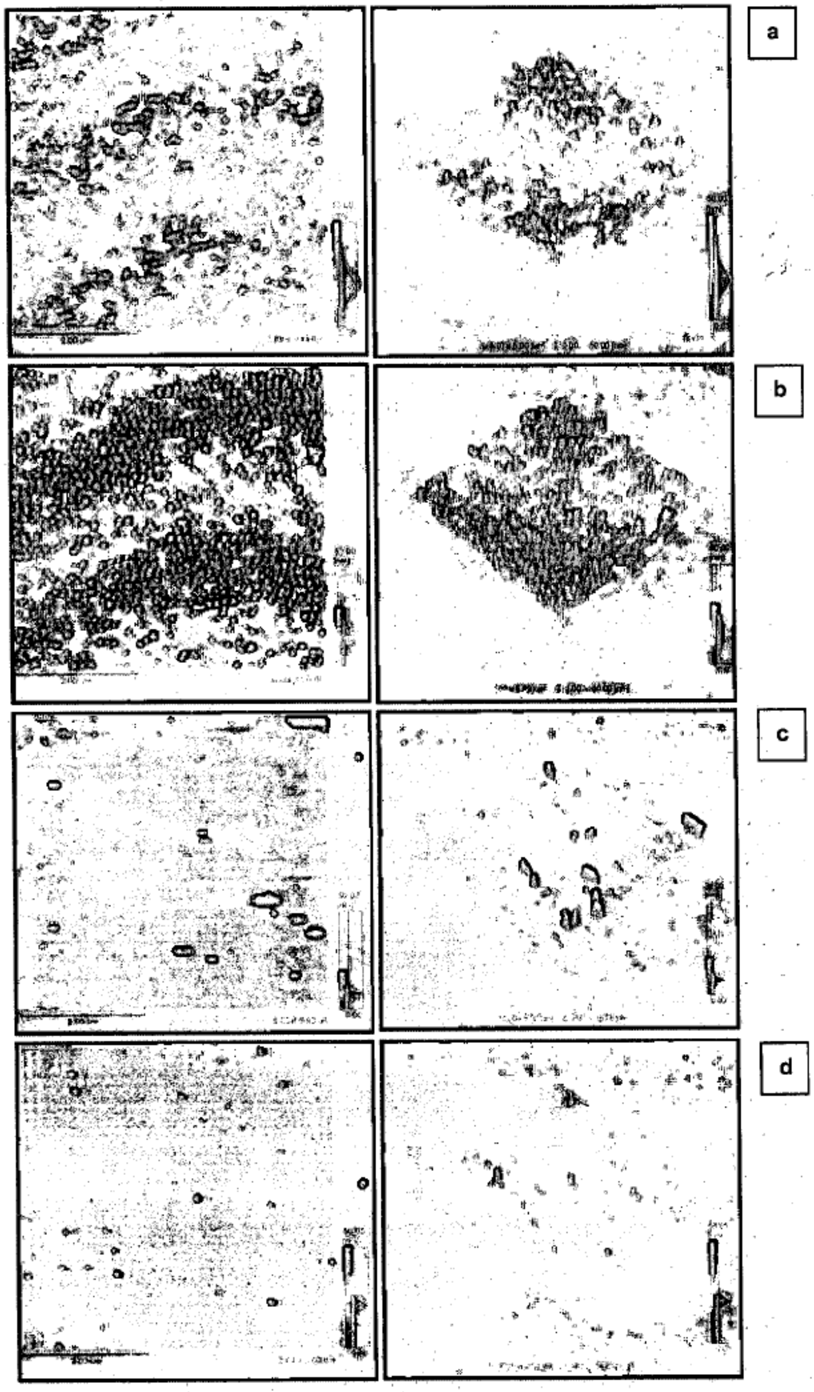

Fig. 13: AFM images for varying filling pressure a) 0.5 mbar b) 1 mbar c) 1.5 mbar d) 2 mbar

Fig. 13 shows the AFM images corresponding to the varying filling pressure. The thin films prepared at lower filling pressure of 0.5 mbar and 1 mbar has continuous network of agglomerated and fused titanium dioxide particle all merged together forming a dense thin film as depicted in Fig 14 (a & b). The thin films prepared at higher filling pressure of 1.5 mbar and 2 mbar represents less number of titanium dioxide particles and have less rough surface as depicted in fig 14 (c & d). The R_{rms} values as a function of chamber pressure are drawn in the fig. 14.

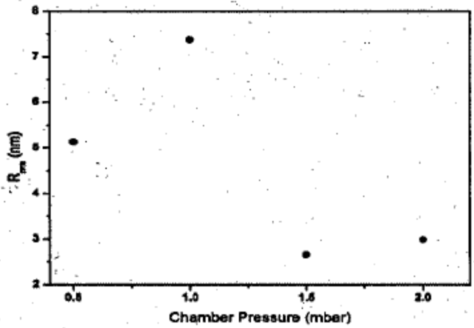

Fig. 14: R_{rms} of the TiO_2 thin films prepared at varying chamber pressure.

4. CONCLUSIONS

Titanium Dioxide (TiO_2) thin films were successfully deposited in silicon (100) and glass substrates by using pulsed dc glow discharge. The argon was used as sputtering gas whereas oxygen was used as reactive gas with ratio of 20/ 80. The operating pressure was varied from 180 W to 240 W whereas filling pressure was varied from 0.5 mbar to 2 mbar with fixed deposition time and inter-electrode distance. The effect of variation in power and pressure on structure, chemical composition and morphology was characterized by XRD, FTIR, SEM and AFM respectively. XRD results show that when TiO_2 is deposited on silicon substrate, the intensity of the original peak of Si (100) at 69° decreases with the increase in power and no extra peak related to any form of titanium dioxide appears. When TiO_2deposited on glass substrate with variation in power shows similar XRD pattern with no extra peak related to titanium dioxide. Similarly titanium dioxide deposited with variation in filling pressure shows similar trend with no peak related to titanium dioxide except small bumps of Si (100) at 69°. The XRD results revel that with the variation in operating power and pressure results in the formation of amorphous titanium dioxide thin films on both silicon and glass substrates. FTIR spectroscopy confirms the presence of titanium dioxide on silicon substrate with strong peaks in the wavenumber range of 700-1000 cm^{-1}.

The SEM results depict that sputtering increases with power resulting in the increased formation of TiO_2 on silicon substrate. Ionized oxygen also oxidizes the substrate and form bubble like structure as visible on the SEM micrographs. The surface morphology of the deposited titanium dioxide thin films at varying filling pressure shows similar spherical, bubble like and flower like structures. AFM results show that all the samples depict almost rough surface composed of closely packed titanium dioxide particles of various grain sizes and root mean square roughness values ranging from 2 nm to 8 nm showing combination of rough and uniform thin films.

Acknowledgements:

We are grateful to Prof. Dr. Saadat Siddiqi, Dr. Abdussamad Khan and Miss Mariam from IRCBM COMSTAS Lahore for providing us FTIR facility.

REFERENCES

1. Myung-Hwan An, Journal of the Korean Physical Society, 47 (2005) 847.
2. C. Giolli, F. Borgioli, A. Credi, A. Fabio, A. Fossati, M. Miranda, S. Parmeggiani, G. Rizzi, A. Scrivani, S. Troglio, A. Tolstoguzov, A. Zoppi and U. Bardi, Surface and Coatings Technology, 202 (1) (2007) 13.
3. M. I. B. Bernardi, E. J. H. Lee, P. N. L. Filho, E. R. Leite, E. Longo and J. A Varela, Materials Research, 4 (2001) 223.
4. A. P. Alekhin, S. A. Gudkova, A. M. Markeev, A. S. Mitiaev, A. A. Sigarev and V. F. Toknova, Applied Surface Science, 257 (2010) 186.
5. W. G. Lee, S. Woo, J. C. Kim, S. H. Choi and K. H. Oh, Thin Solid Films, 237 (1994) 105.
6. M. J. Alam and D. C. Cameron, J. of Sol-Gel Science and Technology, 25 (2002) 137.
7. Y. Jin, G. Li1, Y. Zhang, Y. Zhang and L. Zhang, J. Phys.: Condens. Matter, 13 (2001) L913.
8. W. Kaiser, Phys. Rev., 105 (1957) 1751.
9. http://www.thermo.com.cn/Resources/201007/271120772.pdf
10. C. Voulgaris, E. Amanatides, D. Matarasand, D. E. Rapakoulias, J. of Phys.: Conference Series, 10 (2005) 206.
11. E. F. D. Reis, F. S. Campos, A. P. Lage and R. C. Leite, Materials Research, 9 (2006) 185.
12. I. Safi, Surface and Coatings Technology, 127 (2000) 203.
13. S. Mraz, "Influence of the plasma chemistry and energetics on the composition and structure evolution of sputtered oxide thin films", Materials Chemistry Dissertation no. 07, RWTH Aachen University, Germany, (2006).
14. B. Liua, X. Zhao, Q. Zhaoa and C. L. He, Materials Chemistry and Physics, 90 (2005) 207.

PK ISSN 0022- 2941; CODEN JNSMAC
Vol. 54, (2014) PP 27-36

CURRENT AND FUTURE PROSPECTS OF HIGH TEMPERATURE SUPERCONDUCTING PRODUCTS

MUHAMMAD ASGHAR[1], M. FAROOQ ZAFAR[2] AND SYED ZAFAR ILYAS*[1]

[1]Department of Physics, Allama Iqbal Open University, Islamabad.
[2]NESCOM, Islamabad.

*E-mail address: szilyas@yahoo.com

(Received: 21-01-2015)

ABSTRACT: The first High Temperature Superconductors was discovered in 1987 and till now only very few materials are being used HTS products at commercial scale for example $Bi_2Sr_2Ca_2Cu_3O$ (BSCCO) is only being used in producing commercial – level HTS wire. This research/study was aimed to explore the recent development in HTS and its future prospects in various fields of science and technology e.g. medical, Electronics, Industry, Power Generation and Transportation in modern world. The commercial and large scale production of HTS technology will be boosted as the performance and cost effectiveness of HTS materials are improved. New applications of superconductors will increase with critical temperature. Liquid nitrogen based superconductors has provided industry more flexibility to utilize superconductivity as compared to liquid helium superconductors. The possible discovery of room temperature superconductors has the potential to bring superconducting devices into our every-day lives. At the end some suggestions are given for effective research and development of HTS materials. These suggestions are equally useful for the whole third world countries.

Keywords: Critical temperature, Superconductors.

1. INTRODUCTION

Superconductors are the materials including metals, ceramics and more recently plastics that have zero electrical resistivity at certain temperature called critical temperature T_c. The electrical resistivity of a metallic conductor decreases gradually as temperature is dropped. In ordinary conductors, such as copper or silver, this decrease is limited by impurities and other defects. Even near absolute zero, a real sample of a normal conductor shows some resistance. In a superconductor, as the temperature is reduced, the interaction of the conducting electrons with impurities, defects and the vibrating ions of the lattice also reduced. This phenomenon is called Superconductivity.

The phenomenon of superconductivity requires extremely low temperatures, generally somewhere just above absolute zero (0 degrees Kelvin, -273 Celsius or -459 degrees Fahrenheit). The critical temperature T_c at which electrical resistance in materials is zero varies depending on the material and it is achieved by cooling the materials with either liquid helium (for low temperature superconductors) or liquid nitrogen (for high temperature superconductors).

Electrical resistance in superconducting metals occurs because of the atomic structure of metals - which can be thought of as metallic nuclei swimming in as "sea" of electrons; negatively-charged electrons are not bound to a particular positively-charged nucleus. In normal metal, electrons will move quickly and constantly collide, thus creating heat energy that is why materials are normally at a temperature above absolute zero.

However, in superconducting metals, electrons are greatly slowed down and do not collide into one another. This why superconducting materials do not lose energy - heat is never created because there are no collisions. In superconducting metal, an electron moves through two rows of positively-charged atoms, thus pulling the two rows of atoms inward because of their attraction to the electron. This distortion created then causes another electron to follow behind the first. These two electrons pair up and encounter less resistance overall [1].

2. A BRIEF HISTORY

This fascinating and challenging phenomenon of physics was discovered by Dutch Physicist Heike Kamerlingh Onnes on the 8th April 1911 when he used liquid helium to cool down a sample of mercury. He observed a sudden drop in resistance to an immeasurably small value when the temperature of the sample reached a value below 4.2 K; unfortunately, there was no complete explanation for the event at the time of the experiment because the quantum theory of metal was not yet developed to its full potential. This incredible characteristic of lossless current has attracted strong interest in the field of basic physics and well as in industry [2].

In 1933, another interesting aspect of superconductors was demonstrated by Meissner and Ochsenfeld. When a superconductor, cooled below its critical temperature, was placed in an external magnetic field, the magnetic flux was completely excluded from its interior. This phenomenon is known as the Meissner effect, In terms of electromagnetism, the material in the superconducting state is perfectly diamagnetic. This technology has been practically used as mag-lev (magnetic levitation) technology that can power high-speed trains. Japan had tested this technology in 1999 the MLX01 test vehicle recorded a top speed of 343 miles per hour. In this illustration, strong superconducting magnets cause a transport vehicle to float above a track, thereby excluding resistance and friction, allowing trains to move at higher speeds without wasting energy, by turning electricity into heat electrical energy [3].

Two years later in 1935, the London brothers published a theory to explain the behavior superconductors [4]. According to today's knowledge and understanding of the subject, the London theory was insufficient and could not explain all the aspects of superconductivity. However, it introduced many concepts that are still widely in use, e.g. the *London penetration depth* **λ_L (λ_L** is an ideal theoretical limit that determines how deep into a bulk superconductor material a magnetic or an electric field can penetrate) and London equation. In 1953, Pippard gave extension to London theory. He introduces the concept of coherence length, which is one of fundamental parameters in the theory of superconductivity. It represents the smallest wave packet that the superconducting charge carriers can form [5].

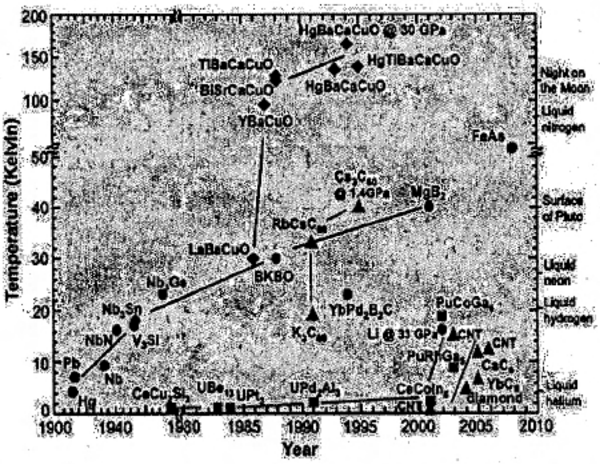

Fig. 1: Evolution of the superconducting temperature Tc since the discovery of the phenomenon [6].

In 1950s and 1960s the theoretical understanding of superconductivity took giant leap. The appearance of Ginzburg-Landau (GL) and Bardeen-Cooper-Schrieffer (BCS) theories in 1950s on the mechanism of superconductivity are evidence of research and development made. Besides Hg, many superconducting materials have been discovered which includes metals, alloys and compounds. Nevertheless, it took half a century to explicate the basic mechanism and to provide the platform for applications until another period started in 1960, which is highlighted by emphasis on applications, and it continues up to now [7].

Before the 1980s, the critical temperature of Nb_3G (Tc = 23.2 K) was considered to be as the highest attainable [8]. However, in 1986 Bednorz and Muller discovered superconductivity in BaLaCuO system which had critical temperature in 30 Kelvin range [9]. A huge amount of effort was made, and soon systems with critical temperature up to 100K were found. The critical temperature of $Sn_1Pb_0In_{0.5}Ba_4Tm_6Cu_8O_{22+}$ is 195 K which is a current world record. However, this material does not form stoichiometrically. The theoretical mechanism of superconductivity in these oxide-class high Tc superconductors and what the BCS model predicts are possibly very different from each other.

3. TYPES OF SUPERCONDUCTORS

Superconductors are divided into in two types, depending on their behavior in an external magnetic field.

3.1 Type I superconductors:

Type I superconductors are those superconductors which lose their superconductivity very easily or abruptly when placed in the external magnetic field. It can be seen from the graph of intensity of magnetization (M) versus applied magnetic field (H), when the Type I superconductor is placed in the magnetic field; it suddenly or easily looses its superconductivity at critical magnetic field (Hc) (point A).

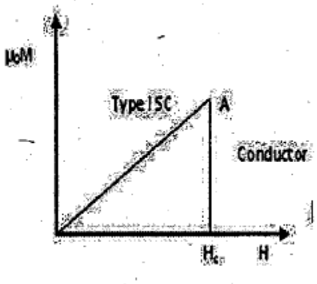

Fig. 2: Type I Superconductors

After Hc, the Type I superconductor will become conductor. These types are also known as **soft superconductors** because of this reason that is they loose their superconductivity easily. Theses superconductors perfectly obey Meissner effect. Examples are Aluminium (Hc = 0.0105 Tesla) and Zinc (Hc = 0.0054).

3.2 Type II superconductors:

Type II superconductors are those which loose their superconductivity gradually but not easily or abruptly when placed in the external magnetic field. As we can see from the graph of intensity of magnetization (M) versus applied magnetic field (H), when the Type II superconductor is placed in the magnetic field, it gradually loses its superconductivity. Type II superconductors start to lose their superconductivity at lower critical magnetic field (Hc1) and completely lose their superconductivity at upper critical magnetic field (Hc2).

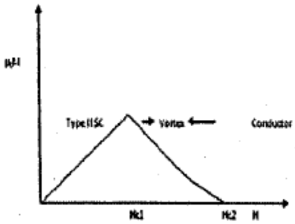

Fig. 3: Type II Superconductors

The state between the lower critical magnetic field (Hc1) and upper critical magnetic field (Hc2) is known as vortex state or intermediate state. After Hc2, the Type II superconductor will become conductor. Type I superconductors are also known as **hard superconductors** because of this reason that is they loose their superconductivity gradually but not easily. Type II superconductors obey Meissner effect but not completely. NbN (Hc = 8 x 106 Tesla), Babi3 (Hc = 59 x 103 Tesla) are the examples of Type-II superconductors. Type-II superconductors are used for strong field superconducting magnets [10].

4. SIGNIFICANCE OF UNIQUE PROPERTIES

Superconductors are different from conventional materials with respect to free electrons or electric currents move through the material. These are the differences that give rise to unique properties and performance benefits that differentiate superconductors from all other known conductors. Lossless current flow and high current density plays an important role in transmission of electric power and also enable much smaller or more powerful magnets for motors, generators, energy storage, medical equipment and industrial separations. There is often a secondary benefit, which makes superconductivity particularly attractive compared with conventional technology. For example, superconductors are smaller, lighter and more efficient than conventional conductor and also allow improvements in processes in some cases. Low resistance at high frequencies and extremely low signal dispersion are key aspects in microwave components, communications technology and several military applications. The high sensitivity of superconductors to magnetic field provides a distinctive sensing capability, in many cases thousand times superior to today's best conventional measurement technology. Magnetic field exclusion is important in multi-layer electronic component miniaturization, provides a mechanism for magnetic levitation and enables magnetic field containment of charged particles. The last two properties provide the basis for digital electronics and high speed computing well beyond the theoretical limits projected for semiconductors. All of these materials properties have been extensively demonstrated throughout the world.

5. AN OVERVIEW OF APPLICATIONS

Superconductivity is exclusive and dominant phenomenon of nature. Nearly 100 years after its first discovery, its full commercial application is just to be started. It is usually regarded as one of the great scientific discoveries of the 20th Century. This amazing property causes certain materials, at low temperatures, to lose all resistance to the flow of electricity. This state of "losslessness" enables a range of innovative technology applications. At the dawn of the 21st century, superconductivity provides the foundation for new commercial applications that are transforming our economy and daily life.

Before 1973 many other metals and metal alloys were found to be superconductors at temperatures below 23.2K. These became known as Low Temperature Superconductors (LTS) materials. Since 1960s a Niobium-Titanium (Ni-Ti) alloy was the material used for commercial superconducting magnets. More recently, a brittle Niobium-Tin intermetallic material has appeared as an excellent alternative to achieve even higher magnetic field strength. In 1986, J.G. Bednorz and K.A Muller discovered oxide based ceramic materials that exhibited superconducting properties as high as 35K. Ceramics tend to be hard and brittle, making their applications somewhat limited at this stage of development. While ceramics don't need to be cooled down as much or with liquid helium, they are difficult to form long flexible wire with. This was quickly followed in early 1987 by the announcement by C. W. Chu of cuprate superconductor functioning above 77K, the boiling point of liquid nitrogen. Since then, extensive research worldwide has uncovered many more oxide based superconductors with potential manufacturability benefits and critical temperatures as high as 135K. A superconducting material with critical temperature above 23.2K is known as High Temperature Superconductors (HTS), despite the continuing need for cryogenic refrigeration for any application.

Nearly fifty years of development and commercialization of applications involving LTS materials have demonstrated that a superconductor approach works best when it represents a unique solution to the need. Alternatively, as the cost to the superconductor will always be substantially higher than that of a conventional conductor, it must bring irresistible cost effectiveness to the system. The advent of HTS has changed the dynamic of refrigeration by permitting smaller and more efficient system cooling for some applications. Design, integration of superconducting and cryogenic technologies, demonstration of systems cost benefits and long term reliability must be met before superconductivity deliver on its current promise of major societal benefit and makes considerable commercial inroads into new applications. The current commercial applications of superconductivity are Magnetic Resonance Imaging (MRI), Nuclear Magnetic Resonance (NMR), High-energy physics accelerators, Plasma fusion reactors and Industrial magnetic separation of Kaolin clay. All these applications involve LTS materials. Indeed, without superconducting technology most of these applications would not be feasible. Superconductor-based products are extremely environment friendly compared to their conventional counterparts. They generate no green house gases and are cooled by non-flammable liquid nitrogen (nitrogen comprises 80% of our atmosphere) as opposed to conventional oil coolants that are both flammable and toxic. They are also typically at least 50% smaller and lighter than equivalent conventional units which translate in to economic incentives. These benefits have given rise to the ongoing development of many emerging applications in the following sectors:

Electric Power: Superconductors enable a variety of applications to aid our aging and heavily burdened electric power infrastructure e.g. in generators, transformers, underground cables, synchronous condensers and fault current limiters. The high power density and electrical efficiency of superconductors wire results in highly compact, powerful devices and systems that are more reliable, efficient and environment friendly.

Transportation: The rapid and efficient movement of people and goods by land and by sea poses important logistical, environmental, land use and other challenges. Superconductors are enabling a new generation of transport technologies including ship propulsion systems, magnetically levitated trains, and railway traction transformers.

Medicine: Advances in HTs promise more compact and less costly Magnetic Resonance Imaging (MRI) systems with superior imaging capabilities. In addition, Magneto-Encephalography (MEG), Magnetic Source Imaging (MSI) and Magneto Cardiology (MCG) enable non-invasive diagnosis of brain and heart functionality.

Industry: Large motors rated at 1000HP and above consume large amount of electricity generated in USA. They offer a prime target for the use of HTS in considerably reducing electrical losses. Powerful magnets for water remediation, materials purification, and industrial processing are also in the demonstration stages.

Communication: Over the past decade, HTS filters have come into widespread use in cellular communications systems. They enhance signal-to-noise ratios, enabling reliable service with fewer, more widely-spaced cell towers. As the world moves from analog to all digital communications, LTS chips offer dramatic performance improvement in many commercial and military applications.

Scientific Research: Using superconducting materials, today leading-edge scientific research facilities are pushing the frontiers of human knowledge and pursuing breakthroughs that could lead to new techniques ranging from the clean abundant energy form nuclear fusion to computing at speeds much faster than the theoretical limit of Silicon technology [11].

Since room temperature superconductivity has not been found yet, the applications of high-temperature superconductivity are constrained to temperatures around that of liquid many attempts to obtain high temperature superconductivity in materials other than cuprates. Superconductivity was observed in alkali-ion doped C_{60} at 33K, and Akimitsu very recently found superconductivity in MgB_2 very recently found superconductivity in MgB_2 at of 39K. But the superconductivity in both these materials is explained by the BCS theory, so it can be said at present that all non BCS superconductors belong to cuprate family. We therefore need to find new non BCS superconductors outside the cuprate family if we raise the critical temperature beyond temperature. Room temperature superconductivity is still a dream of many scientists, but there is no guideline to reach it at present. A little bit of hope, however, may be found when consider organic compounds. The methods for analyzing very complicated biological materials, like the human genome, are developing very fast and it may soon be possible to analyze the interactions between complicated genomes and proteins. This would enable us to simulate new organized materials on high-speed supercomputers and evaluate the interaction between electrons and molecules in new materials. This a way to understand excitonic superconductivity suggested little in 1964. This means the development of future computing science will open a new way for science and technology of new superconducting materials [12].

6. FOUNDATION FOR FUTURE PROSPECTS

The potential of the technology has been identified around the world. Countries such as the USA, Japan, Korea, China and India have increased their research activity. Germany is among leaders, having offered significant research subsidies in the nineties. Medium-sized companies in particular can easily offer highly-developed products and system solutions. In order to maintain and expand this healthy situation, the German Federal Ministry of Economics and Technology promotes the development of the technology and its applications in number of projects. Other early markets are arising where the relative efficiency, size and weight advantages of devices based on high-temperature superconductivity outweigh the additional costs involved.

Favourable future applications include high-performance smart grid, electric power transmission, transformers, power storage devices, electric motors (e.g. for vehicle propulsion, as in vactrains or maglev trains), magnetic levitation devices, fault current limiters, nanoscopic materials such as Bucky balls, nanotubes, composite materials and superconducting magnetic refrigeration. However, superconductivity is sensitive to moving magnetic fields so applications that use alternating current (e.g. transformers) will be more difficult to develop than those that rely upon direct current [13].

7. CONCLUSION

The opportunity for further investigation in the field of high temperature superconductivity sees inexhaustible. Twenty Seven years have already passed since high-temperature superconductivity was discovered in 1986. Many new materials have been found and the critical temperature of superconducting materials has ascended to 135K. To get superconductivity at room temperature, however, we must find materials other than those in the cuprate family. It is very difficult to say when that can be done and who can do it. The theoretical basis of high temperature superconductivity is still uncertain and it must remain in the forefront of solid state physics. On other hand, we can see the future of the superconducting technologies more undoubtedly than ever and can expect the superconductivity industry to take off in upcoming years. It must play an important role in the new industrial revolution now proceeding. It should also be clear that developments other than in superconducting materials themselves e.g. manufacturing processes, insulation, cryogenics, cryorefregeration, and cost reductions - are also supportive and essential for nonstop success in superconducting applications. Unless there is no other way to solve a problem, a superconducting design will always be in competition with other solution processes, which may be more cost effective or dependable. Superconducting materials may contribute to the effort most readily by increasing the available system operating temperature, but the other properties discussed are also critical.

REFERENCES

1. D. Halliday, R. Resnick and J. Walker, Fundamentals of Physics, 6th ed., John Wiley and Sons, New York (2000).
2. M. Tinkham, Introduction to Super-conductivity, 2nd ed., McGraw Hill, New York (1996).
3. H. McGeory, Superconductivity Transmission through Superconductor Technology, Global Change Associates, (2004).
4. F. London and H. London, Proc. Of Roy. Soc. Of London, A149 (866) (1935) 71.
5. A. B. Pippard, Proc. Of Roy. Soc. Of London, A216 (1127) (1953) 547.
6. http://en.wikipedia.org/wiki/History_of_superconductivity.
7. R. Jarvinen, K. Kacprzak and S. Valtonen, Superconductivity and High Tc Superconductor $YBa_2Cu_3O_{7-x}$, Advanced Laboratory Work FYSZ460, (2008).
8. J. X. Jin and S. X. Dou, Science & Technology Advancing into New Millenium, (1999) 368.
9. S. Elliot, The Physics and Chemistry of Solid State Physics, John Wiley and Sons, New York (1998).
10. J. G. Bednorz and K. A. Muller, Z. Phys. B – Condensed Matter, 64 (1986) 189.
11. http://www.winnerscience.com/superconductivity/type-i-and-type-ii-superconductors/
12. http://www.ccas-web.org/pdf/ccas_brochure_web.pdf
13. S. Tanaka, Japan Society of Applied Physics International, 4 (2001) 17.

PK ISSN 0022- 2941; CODEN JNSMAC
Vol. 54, (2014) PP 37-57

NEW CASTING STRATEGY FOR ELIMINATING BOTH INDIGENOUS AND EXOGENOUS GAS POROSITY WITHIN THE MOULD

PERVAIZ HABIBULLAH*[1], MIAN AHSAN MAHMOOD[1], ZEESHAN ANWAR[1], M.M. PARIONA[2]

[1]22-Davis Road, Lahore, Pakistan.
[2]Ponta Grossa State University, Ponta Grossa, Brazil.

*E-mail address: drpervaiz.h@hotmail.com

(Received: 15-09-2014)

ABSTRACT: A phenomenal success has been obtained in eliminating the casting defects, within the mould cavity, by utilizing a new casting strategy which comprises: (i) scavenging the gas dissolved in the melt and mould gas by flushing with Argon, introduced at an adequate pressure in the sand mould cavity (gentle stirring rate <5scfm) and then (ii) absorbing the mould gas and Argon mixture from the mould by imposing soft vacuum -25 to -75 torr. First, the numerical simulation of the casting: Railway wagon brake, was conducted by CAE (finite element method) and hot spots were identified. The gate was placed near the hot spots to avoid the defects due to stress development during casting (i.e. hot and cold tears). For imposition of vacuum a specially designed double lined flask is used: its internal lining is finely perforated while outer shell is solid and is connected in the vacuum pump through an orifice. Space between two linings is ½ to ¾ in. Argon is introduced at adequate pressure in the mould cavity immediately after pouring by an outfit specially designed for this purpose and then vacuum is imposed on sand mould by turning on the vacuum pump. This casting strategy eliminates the gas porosity in casting in four stages. (1) at commencement of pouring, large volume of gas appears which is flushed by Argon (flushing) (2) on imposing of vacuum the mould gas mixture and air in pores of the mould is absorbed by vacuum (absorption) (3) as casting solidifies, it contracts. Air gap is widened while the sand grains dilate decreasing the permeability of the mould (widening of air gap) (4) air from the air gap of the mould is, first, replaced by the mould gas then by air (evacuation and filling). Argon scavenges any gas dissolved by the liquid metal, as well as mould gas, while the '*depression*' created by vacuum sucks all the gas in the mould. In this way, both indigenous porosity (appearing by dissolution and precipitation of gases during solidification) and exogenous porosity (produced by penetration of gas coming from mould and metal-mould interface) are eliminated, within the mould. Besides combating gas porosity, this casting technique offers a number of other advantages. When air gap and pores of the mould are filled with Argon (or gas mixture with great percentage of Argon) 'secondary oxidation' within the mould cavity and oxidation reactions at metal mould interface are retarded. It is a confirmed fact that oxides are main source of casting defects: when oxides react with carbon, form carbon monoxide (main source of gas porosity in steel) while reaction of FeO with SiO_2 sand, forms fayalite (creating sand burn-on) and when FeO wets the sand grains, it increases wetability of liquid steel), making a way for metal penetration. Presence of Argon in mould pores plays an important role in combating these defects because it retards these reactions being an inert gas. Sound Railway wagon Brake and Brake disc of automobiles were cast by utilizing this casting strategy. Gas porosity of these castings was totally removed by utilizing the said casting strategy. Further studies on combating hot and cold tears by applying this casting technique may be carried out.

Keywords: Exogenous and Indigenous gas porosity, Simulation, Flushing by Argon, Vacuum imposition and Mechanism of Elimination.

1. INTRODUCTION

Gas porosity in casting is an outcome of evolution of gases from:

- Substances present in the moulding material (water, additives, minerals in silica sand etc.) and Liquid metal/mould interaction.
- Liquid metal, gases which are absorbed during melting and casting.

Depending upon the origin of gases, the gas porosity is grouped in:

- Exogenous -- formed by gases produced from the mould by metal and mould interaction. These comprise evaporation of water and volatile substances, burning of organic material, decomposition of minerals, dissociation of gases, dilation of air present in the pores of the mould, decomposition of organic substances and other physico-chemical reactions taking place at alloy mould interface.
- Indigenous -- produced by the atmospheric gases dissolved in liquid metal and their reactions within the volume of liquid metal during melting, pouring and solidification. Most of the researchers have suggested that indigenous porosity is the consequence of normal segregation of dissolved gases ahead of solidification front and the normal processes of 'nucleation' and growth of the pores from gases in solution in metal.

1.1 Mechanism of Exogenous Gas Porosity Appearance:

Exogenous porosity is formed in following three steps:

- Appearance of supplementary gas pressure at the liquid alloy-mould interface.
- Penetration in gas bubble in the liquid alloy.
- Fixation of gas bubble in casting wall forming porosity.

The bubble of gas penetrates in liquid alloy when

$$P_f > P_m + P_c + P_{atm} + P_s$$

Where P_f is gas pressure at alloy-mould interface, P_m – metallostatic pressure, P_c – pressure necessary for overcoming capillary forces ($P_c = 2\sigma \cos\theta / r$ where σ = surface tension of liquid alloy, θ = contact angle, r = radius of pore in mould surface). P_{atm} – atmospheric pressure and P_s - pressure of gas formed in the mould cavity, on the rising surface of the liquid metal (gases evolved during the mould filling may float over casting putting pressure on the level of liquid rising in mould cavity).

Recently, casting simulation has been increasingly used for predicting gas porosity. For this reason many studies on mould filling and solidification analysis in casting processes have been conducted. The simulation results of such a recent study on gas entrapment shows that many small gas defects will occur separately from the large entrapment defects and will generally concentrate in the center of the mould cavity [10].

1.2 Mechanism of Exogenous Gas Porosity Appearance:

Hydrogen concentration and the total amount of nitrogen and oxygen in cast iron are mainly affected by melting method. The hydrogen concentration is also sensitive to the dwell time in ladles and furnaces and at least directly affected by temperature. The total amount of oxygen is significantly affected by temperature, and the dissolved amount of oxygen shows a strong relationship with temperature. Investigations carried by Orlenius et al [9] show the concentration of all the three gases in the molten iron was found below solubility limit during melting and transportation, but the hydrogen and nitrogen are absorbed during the mould filling and in some cases, raised to levels close to the maximum solubility concentration.

The dissolution and diffusion of H_2 in liquid metal adjacent to solidifying front has been explained by J. Campbell, 1991 [2]. Hydrogen from a surface reaction can diffuse sufficiently far in the time available during the solidification of an average casting to contribute to the formation and growth of sub surface porosity. The salutes are rejected ahead of the advancing solidifying front gradually building up to a concentration peak. Thus conditions are exactly optimum for the creation of maximum gas pressure in the melt at the point a millimeter or so under the surface of casting: the high peak will favour conditions for nucleation of pores; the closeness to the surface will favour the transport of additional gas. If there is enough gas already present in the melt, then contributions from any surface reaction will only add to the already existing porosity. The nucleation of the gas is of two types homogenous and heterogeneous. The gas bubbles growing from the bulk liquid will grow like an atom at a time, as a result of statistical thermal fluctuation, small bubbles with radii less than a critical radius will tend to disappear. A long chain of favourable energy fluctuations will produce a bubble exceeding the critical radius which will have the potential to grow to an observable size. This is homogenous nucleation of bubble while some inclusions, solid surface of an impurity, foreign substrates may become the favourable site for nucleation. This type of nucleation is heterogeneous nucleation. Good nuclei for pore must be non wetting. The pressure required for homogenous nucleation is extremely high while the pressure required for heterogeneous nucleation is much less, almost one twentieth of the pressure for nucleation in bulk liquid (J. Campbell, 1991).

Titanium (Ti) has long been recognized as very helpful in reducing the nitrogen related porosity. 70% FeTi and 0.05% Zr as FeSiZr have also proved highly potent in reducing such porosity [19]. Similarly some composite deoxidizing agents (such as Ti.Al.CaMgSi) have been put forth for reducing indigenous porosity caused by oxygen, nitrogen and hydrogen [23]. The deoxidation is carried out by this deoxidizing agent, in three steps: (1) with FeTi- in furnace (2) by Al – added in ladle just after tapping (3) by CaMgSi – added in ladle just before pouring in mould. Ti reduces the N related porosity Al deoxidizes the oxygen dissolved during melting while CaMgSi added just before pouring reduces the oxygen dissolved due to the 'reoxidation' during transportation and 'secondary oxidation' in the mould cavity. Calcium reduces Phosphorous and Sulphur level in the melt and burning of Magnesium, due to the exothermal reaction, maintains the fluidity.

Table: 1 Pressure thresholds of gas porosity and other related cavitie defects [17].

Defect	Liquid feeding	Gas	Stress	Cavity shape	Criteria	Reference
Exogenous gas porosity	y	y	--	Regular	$P_f > P_m + P_c + P_{atm} + P_s$ $P_f > P_m + P_c$	P. Habibullah (1985) [24] 2011 [2] K Kubo and RD Pehke (1985)
Indigenous gas porosity	y	y	--	Regular	$P_i > P_e$	P. Habibullah (1985) [24] 2011 [2]
Shrinkage microporosity	y y	y –	-- y	Irregular Irregular	$P_f > P_e + P_c$ & $P_e < P_v$	A.S. Sabau & Viswanathan (2002)
Hot tearing	y	–	y	Irregular	$P_e < P_v$	Rappaz Drezet Gremaud (1999)
Hot tearing	y	y	y	Irregular	$P_f > P_e + P_c$	Grandfield, Davidson & Taylor (2001)

Here P_f is the gas pressure (at metal mould interface), P_m is metallostatic pressure (on mould surface), P_c is pressure necessary to overcome capillary forces due to surface tension of the mould surface, P_s is gas pressure on the rising surface of the liquid metal, in the mould cavity, P_{atm} – atmospheric pressure, (total external pressure $P_{ext} = P_{atm} + P_s$), P_e is pressure in the liquid metal, P_i is pressure required to create gas / vapour bubble and P_v is pressure when shrinkage porosity appears.

Table 1 tabulates the pressure thresholds on which gas porosity and other related cavity defects occur. A number of researchers discuss in detail the micro gas porosity transition to the shrinkage porosity. The onset of shrinkage porosity was considered to be the instant at which the liquid metal pressure drops below its saturation, or cavitation value, (P_v). Shrinkage pores typically nucleate heterogeneously from pre-existing bubbles associated with oxide other inclusions and small cavities in the mould walls. The radius of curvature, when porosity forms, is a function of the nature, size and geometry of nucleation site (Sabau et al. (2002) and Kent et al. 2009).

2. Numerical Simulation

Before casting the numerical simulation of the casting: Railway wagon brake (fig. 1), was conducted by CAE (finite element method) and hot spots were identified. The gate was placed near the hot spot to avoid the defects due to stress developed during solidification (i.e. hot and cold tears). The characteristics of material are shown in table 2.

Table 2: Properties of materials

Properties	**Values**
Moulding sand	
Density (kg/m³)	1370
Specific heat (J/kg.K)	1030
Thermal conductivity (W/mK)	0.4
Cast iron	
Composition	**%age**
C	3.3%
Si	2.16%
Mn	0.67%
P	0.02%
Cr	0.13%
Mo	0.29%
Ni	0.1%
Cu	0.31%
Thermal conductivity (W/mK)	
600°C	37.08
800	33.13
1000	36.47
1100	38.1
1200	37.2
1400	33.7

Numerical simulation was carried out by Marriala Consultants Engineering and Software Solutions (ProCast Registered Software) the simulation is based on three fundamental equations for mass, momentum, and energy balance. These equations, expressed in a differential form and referred to as Navier-Stokes equations, are given below. The first one is for continuity, the next three for momentum along x, y, and z directions respectively, and the last for energy. Constant value of density (with respect to temperature) is assumed.

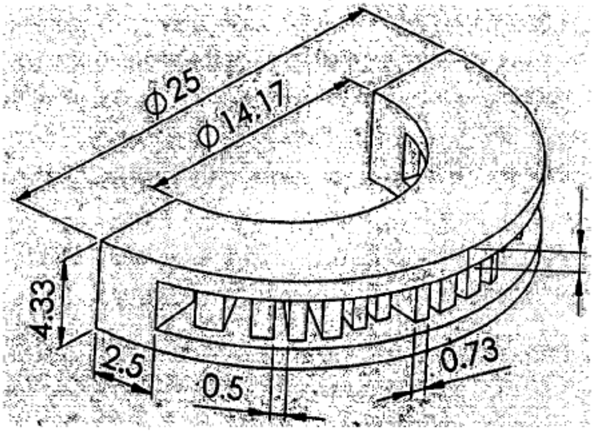

Fig. 1: Railway wagon brake disc (dimension in inches)

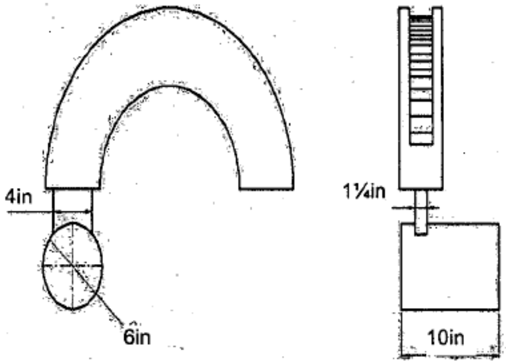

Fig. 2: Location of gate near the hot spots and its dimension (on which numerical simulation is carried out)

Continuity Eq.

$$\frac{\partial v_x}{\partial x}+\frac{\partial v_y}{\partial y}+\frac{\partial v_z}{\partial z}=0$$

Momentum Eq.

Along x – direction

$$\frac{\partial v_x}{\partial \tau}+v_x\frac{\partial v_x}{\partial x}+v_y\frac{\partial v_x}{\partial y}+v_z\frac{\partial v_x}{\partial z}=-\frac{1}{\rho}\frac{\partial p}{\partial x}+\gamma\left[\frac{\partial^2 v_x}{\partial x^2}+\frac{\partial^2 v_x}{\partial y^2}+\frac{\partial^2 v_x}{\partial z^2}\right]+g_x$$

Along y – direction

$$\frac{\partial v_y}{\partial \tau}+v_x\frac{\partial v_y}{\partial x}+v_y\frac{\partial v_y}{\partial y}+v_z\frac{\partial v_y}{\partial z}=-\frac{1}{\rho}\frac{\partial p}{\partial y}+\gamma\left[\frac{\partial^2 v_y}{\partial x^2}+\frac{\partial^2 v_y}{\partial y^2}+\frac{\partial^2 v_y}{\partial z^2}\right]+g_y$$

Along z – direction

$$\frac{\partial v_z}{\partial \tau}+v_x\frac{\partial v_z}{\partial x}+v_y\frac{\partial v_z}{\partial y}+v_z\frac{\partial v_z}{\partial z}=-\frac{1}{\rho}\frac{\partial p}{\partial z}+\gamma\left[\frac{\partial^2 v_z}{\partial x^2}+\frac{\partial^2 v_z}{\partial y^2}+\frac{\partial^2 v_z}{\partial z^2}\right]+g_z$$

Energy Eq.

$$\frac{\partial T}{\partial \tau}+v_x\frac{\partial T}{\partial x}+v_y\frac{\partial T}{\partial y}+v_z\frac{\partial T}{\partial z}=\frac{K}{\rho}\left[\frac{\partial^2 T}{\partial x^2}+\frac{\partial^2 T}{\partial y^2}+\frac{\partial^2 T}{\partial z^2}\right]$$

The equations are solved using finite element method such as Marker and Cell. Simplified marker and cell and solution algorithm-volume of fluid. It divides mould model into a number of cells, which are classified as empty, full and surface cells. A set of imaginary markers is introduced into the system to represent the location of fluid at any instant. A cell is empty if it contain no marker, full when it contains at least one marker and all the cells surrounding it also contain one marker; and is a surface cell when it contains at least one marker and at least one cell surrounding it contains no marker. This method uses fluid function values F to classify the cells. A cell is considered empty when F = 0, full (or interior) when F = 1, and surface cell when F has an intermediate value.

For an interior cell mass of the metal flowing into the cell equals the mass flowing out of the cell and change of momentum equals momentum-in minus momentum-out. For a surface cell, tangential stress on the free surface is zero and normal stress is equal to sum of applied pressure and surface tension (Ravi et al., 2011, Pariona et al., 2008 [8]).

2.1 Mould Filling

Simulation of filling process of a sand mould used for casting of Railway wagon brake (molasses mould, molten metal: cast iron, casting temperature 1400°C).

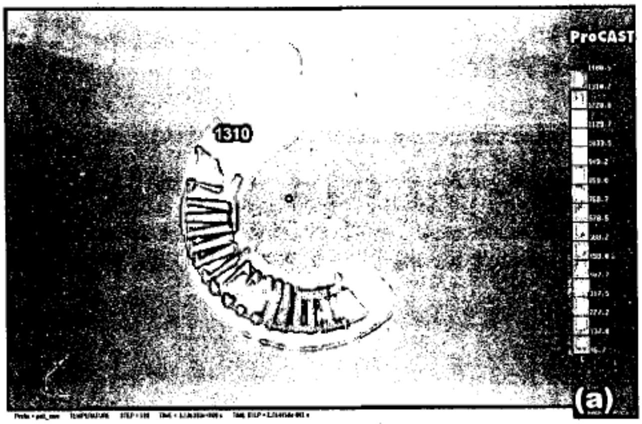

Fig. 3 (a): Mould filling visualized at approx. 3s after pouring. The molten metal emerges from the gate in the form of the 'jet'

Filling of the mould, as revealed by snaps, taken at different time intervals, during casting simulation (by Procast CAE), of Railway wagon brake (for dimension see fig. 1) casting temperature 1400°C, casting velocity 1m/sec, mould wall temp. taken as 50°C).

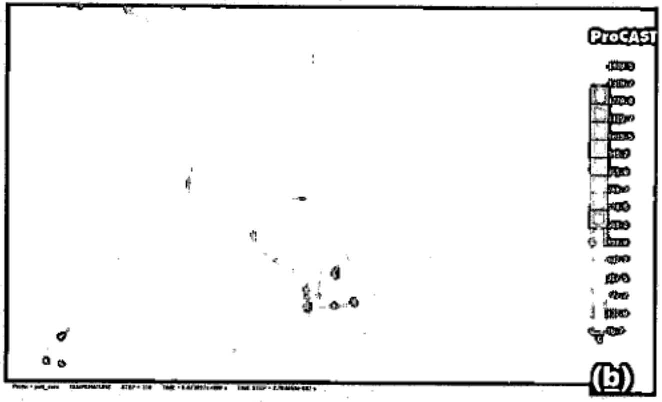

Fig. 3 (b): Mould filling visualized at approx 6s after pouring. The jet of molten metal takes the form of 'stream'.

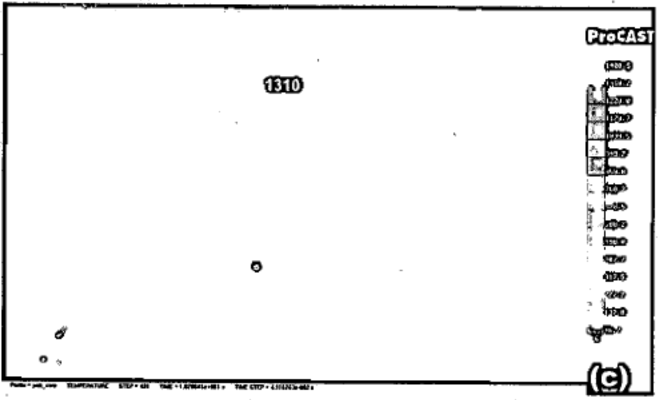

Fig. 3 (c): The front of the stream strikes with the mould wall and mould cavity is completely filled layer by layer, in approx 10s after pouring. So filling time of the casting is approx 10s

2.2 Solidification process and identification of hot spots

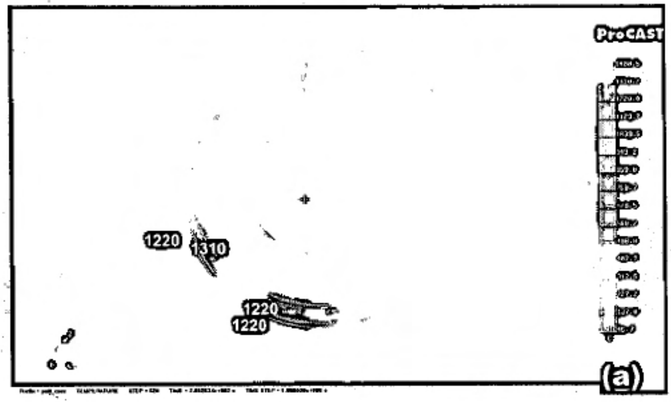

Fig. 4 (a): Solidification starts and hard skin is formed at the curved portion of the casting at approx 200s after pouring.

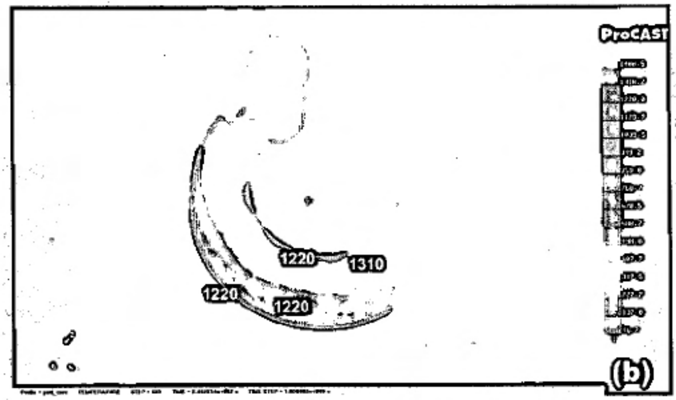

Fig. 4 (b): Solidification front progresses towards interior of the casting (simulation at approx 250s after pouring)

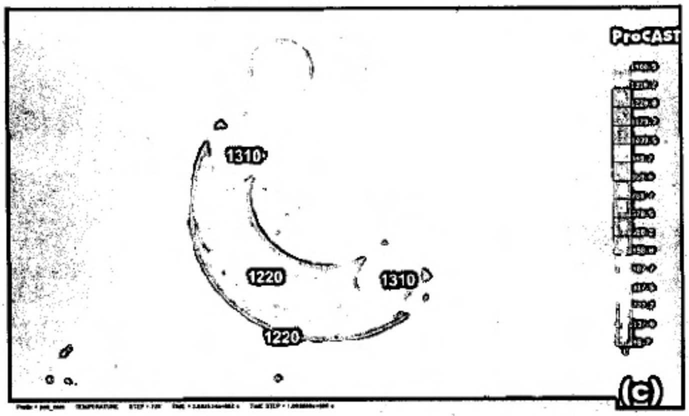

Fig. 4 (c): All the casting is solidified at approx 300s after pouring. Thick portions are solidifying at the end.

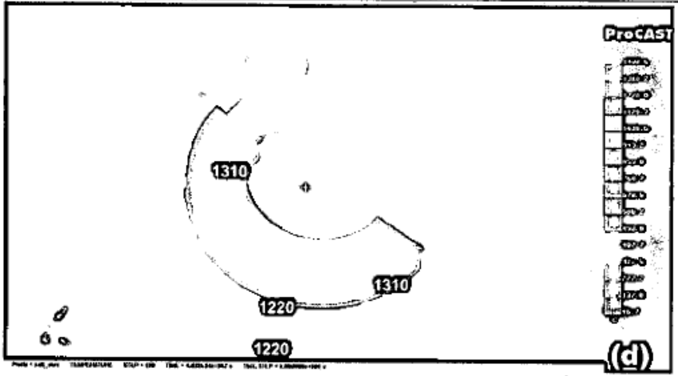

Fig. 4 (d): Solidification at approx 400s after pouring. 'Hot spots' are identified at the thick portion. The gate will be placed near thez hot spots.

2.3 Solidification time

(a) Solidification time of 'hot spots' is almost half an hour.
(b) Metal within the core slots solidification time is approx 40 min.
(c) Solidification time rest of the casting is approx 25 min. **[fig. 5]**.

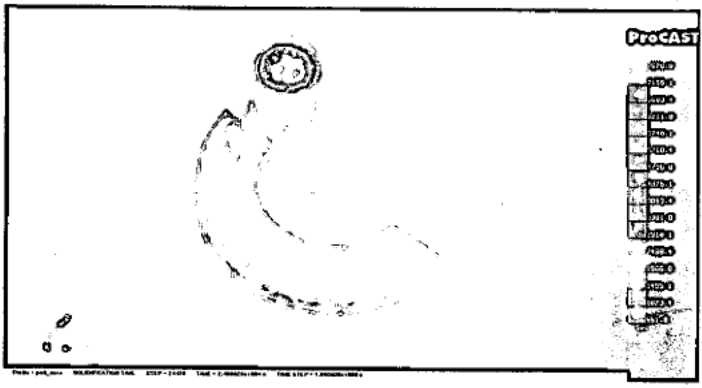

Fig. 5: Simulation of complete solidification time of casting

2.4 Effective stress

Effective stress is simulated 'nil' throughout the casting

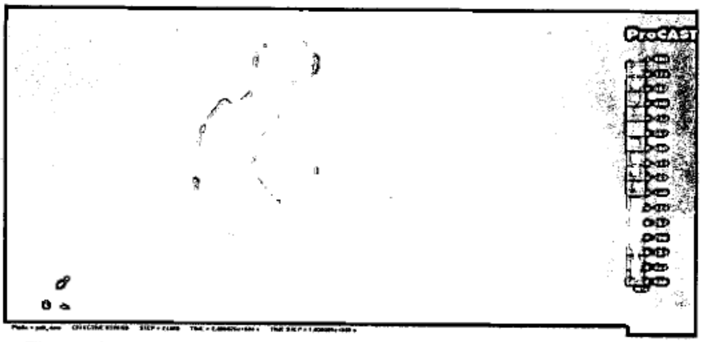

Fig. 6: Simulation of effective stress developed during solidification

3. NEW CASTING STRATEGY

There are a number of interdependent measures which may be applied in the foundry industry for eliminating the exogenous porosity such as, adjusting the binder ratio in the moulds and cores reducing the amount of hydrogen and nitrogen bearing components, pouring at the adequate casting temperature (higher casting temperature increases porosity chances), treating the sand with 10% solution of sulfuric acid followed by water wash and dry and some other techniques [19]. We have suggested that this type of porosity cab be eliminated by imposition of vacuum on the sand mould, making possible reduction in gas pressure at liquid metal / mould interface. In this way we are capable of reducing the gas pressure without changing the nature of the mould. In mould cavity the gas pressure attains the maximum value two times: Ist maximum pressure immediately after pouring and 2nd maximum pressure almost 100-200s after pouring. When sand mould is subjected to vacuum the *depression* is observed and negative pressure appears in it.

The indigenous porosity is eliminated by flushing the mould gas and the gases dissolved in the molten metal by scavenging with Argon. Immediately after flushing when the vacuum is imposed, it sucks the mixture of Argon and mould gas. In this way, both **indigenous** porosity (appearing by dissolution and precipitation of gases during solidification) and **exogenous** porosity (produced by penetration of gas coming from mould and metal-mould interface) are eliminated, within the mould cavity.

In present researches we have applied a casting strategy comprising above mentioned techniques, to eliminate both indigenous and exogenous porosity from heavy castings, such as, Railway wagon brake discs (also called the friction plates) (See fig. 1) cast from gray cast iron at Loco Shop, Pakistan Railways, Lahore, Pakistan and the medium sized casting, such as Brake disc of heavy automobiles.

3.1 Pattern Making:

Pattern made from aluminium was used for casting. Pattern made from aluminium was utilized because in mass production, it does not wear and as such accurate dimension of the final product are assured. It is provided with fine pins for ejecting it from the sand mould. These facilitate, not only the easy drawing of the pattern, from the mould but also avoid certain casting defects crush, misrun etc.

3.2 Moulding:

3.2.1 Specially designed mould box:

Specially designed double lined mould box, provided with a perforated thin steel plate, covered with a steel gauze connected with vacuum pump through a hole in the mould box wall, was used for casting (fig.7). A vacuum pump connected with outer side of the mould box absorbs the gases evolved in the mould cavity, from the time of pouring upto solidification. On the other side of the mould box edge, a hole is perforated from which Argon gas is introduced at an adequate pressure (max. 2000psi) for flushing the gases dissolved in the molten alloy and scavenging the gases evolved in the mould cavity just after pouring. When scavenging and evacuation will be applied together on the mould, the gases dissolved in the molten metal and those ejected in the mould cavity and present in the pores of the mould wall, will be sucked out and will not enter in the solidifying casting.

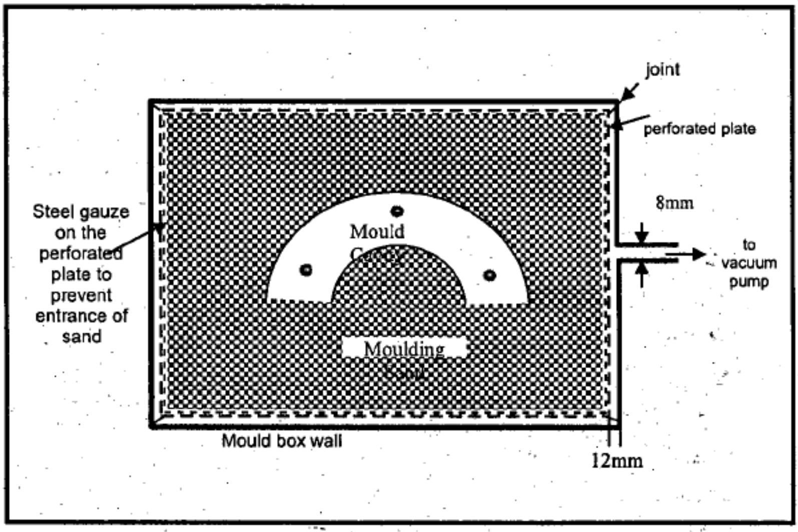

Fig. 7: Specially designed double lined moulding box used for imposing vacuum ('depression') [1, 24].

3.2.2 Moulding sand:

Moulding sand mixture was prepared by using molasses as a special additive and moulding was carried out in specially designed mould box, exactly, in the same manner as in case of conventional sand moulding. The gate is provided near the hot spots as guided by casting simulation (see fig. 2). Pattern is meticulously taken out from the mould and it is done by holding the pins provided with the pattern and drawing it out. Both cope and drag are baked in a baking oven at 350-375°C.

3.2.3 Core fixing:

Wagon brake discs are hollowed out with fins joining together the discs to contact surfaces usually include as part of the casting process. This ventilated disc design helps to dissipate the generated heat while applying brakes. These slots are cast by providing sand cores. These cores are prepared in the core box. Cores are baked in core oven at 350 to 375°C and before pouring they are fixed in the mould cavity, where cores prints are provided for supporting the cores. The core used is made by adding molasses as a binding material in sand.

When cope and drag have been prepared, gate and riser of the required size are provided and core is fixed. Both cope & drag and core are re-heated for some time, for complete drying and ejection of any suspected moisture in the mould and core.

3.2.4 Casting:

3.2.4.1 Composition of alloy cast:

Brake discs are commonly manufactured from gray cast iron. For our experiments we have cast, cast iron of the composition given in table-1.

3.2.4.2 Melting:

Gray iron of above mentioned composition is taken from cupola furnace of 5 ton capacity using mixture of pig iron, cast iron scrap, hot coke (fuel) and lime stone (flux) as charge. Pig iron & scrap, coke and lime stone are charged in layers. The heat is tapped at 1400°C, after each 3 / 4 hours. The ladle which is used for fetching the molten metal is properly heated before tapping. Fe.Si is added in the ladle to diminish the oxygen level in the molten alloy (70% FeTi & 9% Zr in form of FeSiZr are also recommended [9]). The tapping temperature, before transferring the ladle upto the mould line is always 30-50°C higher than the casting temperature so as the adequate fluidity of molten iron is obtained.

3.2.5 Evacuation and Scavenging:

Outfit used for casting of Railway Wagon Brake by imposing vacuum ('depression') through double lined cope & drag and super imposing Argon while pouring is shown in fig. 8. The regulator of the Argon cylinder is turned on and Argon gas is introduced in the mould at an optimum pressure (max. 2000psi) for 1 or 2 seconds (gentle stirring rate <5scfm) and liquid metal is poured. Immediately, the vacuum pump (max. $-1\text{kgf/cm}^2 = -1\text{daN/cm}^2$) is turned on. Take precautions that nozzles should be preheated to prevent the nozzles from acting as heat sinks at the beginning of casting, to avoid thermal shock and clogging [20, 21, 26]. The use of ceramic fiber insulation for manufacturing nozzles has recently been suggested by Nakamura et al. (1995) to avoid the heat loss, clogging and thermal shock. Argon will scavenge all the gas produced in the mould cavity and will flush any gas dissolved in liquid iron. The mixture of the gas collected in the mould cavity, spontaneously after pouring and that of produced in the mould wall will ultimately be sucked by the vacuum pump.

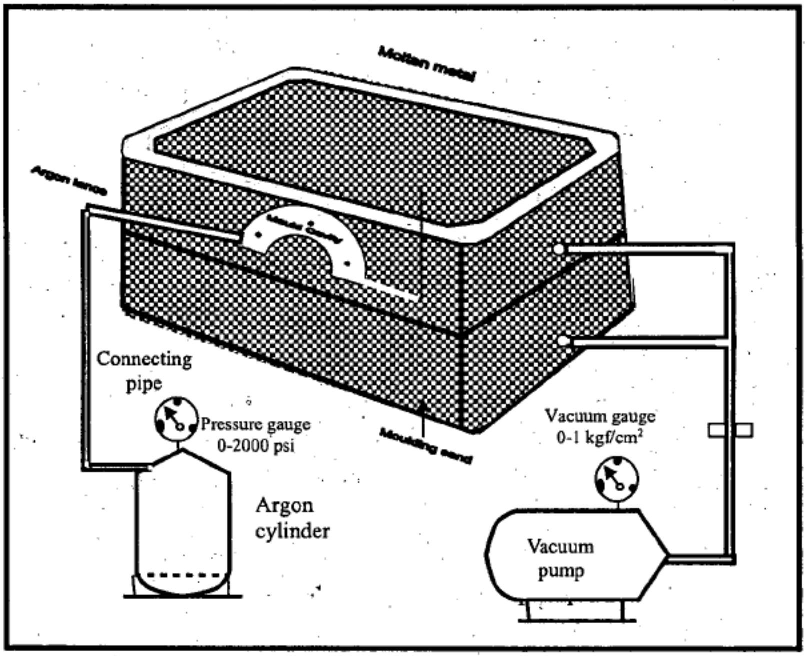

Fig. 8: Outfit used for casting of Railway Wagon Brake by imposing vacuum ('depression') through double lined cope & drag and super imposing Argon while pouring.

3.2.6 Solidification:

The vacuum pump will remain in operation up till the complete solidification and cooling to the room temperature. After cooling to room temperature the sand mould is shacked out and casting of the wagon brake disc is sent to the fettling shop for cleaning.

3.2.7 Fettling:

The gate and riser the casting are removed and it is 'shot blast' for removal of any adheres with the casting surface. The casting then machined as per requirement for giving it the final shape for fixing it on the Railway wagons.

4. MECHANISM OF ELIMINATION OF GAS POROSITY

Argon is introduced at high pressure in the mould cavity immediately after pouring and then, vacuum is imposed on the sand mould by turning on the vacuum pump. The casting strategy put forth eliminates gas porosity in four stages:

1. **Flushing:** During casting in classical sand mould, gas groups are found in molten metal flowing on the mould surface, mould cavity which is empty and

the sand mould itself [10] (fig. a, 9). Flushing involves the creation and dispersion of fine bubbles in the molten metal by introducing Argon gas into a turbulent flow region during pouring. The highly turbulent metal flow splits the gas into the fine bubbles and results in good mixing between the gas and the molten metal phase. Gases, such as, [H], [O], [N], dissolved in the liquid metal, are also transferred to the Argon gas bubbles and removed from the solution [7, 27]. Simultaneously, large volume of gas produced by the mould, at the commencement of pouring is flushed by Argon gas (fig. b,9). Argon also flushes the non metallic inclusions. Inclusions may are formed by reaction of gases with the molten iron or iron oxide. The physical modeling of gas bubbling through the molten metal, carried out by Rogler et al. [15] shows that bubbles smaller than 1mm in diameter are required for maximum separation efficiency of inclusions, while Rogler et al. [16] have found that maintaining bubble size in the range of 0.5 to 3mm should enhance the inclusion removal efficiency. The computation results presented by Joo et al. [22] show that due to convection current created, the mixing upper and lower layers of the molten metal, substantial heat flow losses take place but are of less intensity in case of slopping walls. Small inclusions (e.g. <40μ) are not readily removed on account of their low Stoke's rising velocities.

2. **Absorption:** On imposition of vacuum, the mould gas mixture and air in the pores of the mould is absorbed by the vacuum. It makes possible reduction in gas pressure at liquid metal mould interface without changing the nature of the mould. The inequality $P_f > P_m + P_c + P_{ext}$ changes to $P_f < P_m + P_c + P_{ext}$ thus avoiding the chances of the mould gas to enter the solidifying casting (fig. c, 9). Similarly the '*depression*' exists in the core fixed in the mould cavity [1].
3. **Widening of air gap:** A narrow air gap inevitably exists between metal and the mould wall. The air gap acts as an insulating layer between molten metal and the mould. As the casting solidifies, it contracts. Air gap is, thus, widened. Air gap nucleation depends upon the mould topography and mould thermal conductivity. Higher is the mould conductivity, the quicker the air gap nucleates along the metal-solid shell interface, while composition of alloy being cast has small effect on air gap evolution (L. Tan & N. Zabaras) (Konopka et al. 2007 [11]) (fig. d, 9).
4. **Evacuation and filling:** Air from the air gap is evacuated by imposition of vacuum: air is replaced first, by mould gas mixture and then, by Argon. Similarly the air from the pores of the mould is first, replaced by the mould gas, then, by Argon and ultimately by air. Argon scavenges any gas

dissolved and non-metallic inclusions present in the liquid metal while the 'depression' created by the vacuum sucks all the mould gas mixture. In this way both indigenous and exogenous gas porosity is eliminated within the mould cavity.

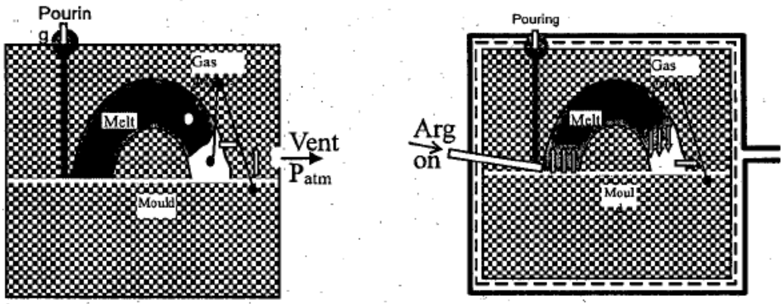

(a) Classical sand mould with vent holes

(b) Flushing of gas from the molten metal and mould cavity

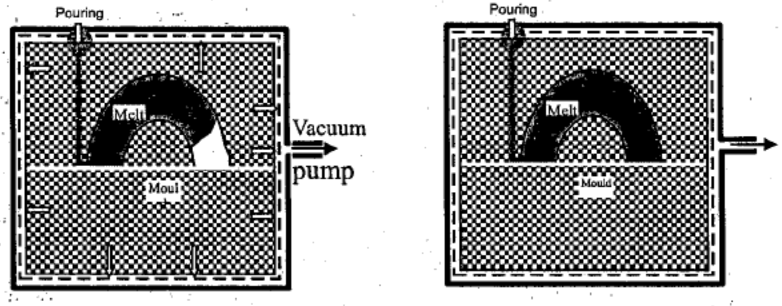

(c) Absorption of gas from mould by imposition of vacuum ('depression')

(d) Elimination of all the gas groups and solidification of casting under vacuum depression

Fig. 9: Schematic illustrating the gas groups in the mould and steps for their elimination by applying the casting strategy put forth (a) the gas groups present in the classical sand mould, based on some bonding material, provided with vent holes. These are found in melt, mould gas in mould cavity and sand mould (b) flushing of gas evolved in the mould cavity and that dissolved in the molten metal by introducing Argon at an adequate pressure (c) absorption of gas generated in the mould by imposition of vacuum in doubled lined flask (d) imposition of vacuum during solidification of the casting.

When air gap and pores of the mould are filled with Argon (or gas mixture with great percentage of Argon) 'secondary oxidation' within the mould cavity and oxidation reactions at metal mould interface are retarded. It is a confirmed fact that oxides are main source of casting defects: when oxides react with carbon, form carbon monoxide (main source of gas porosity in steel) while reaction of FeO with SiO_2 sand, forms fayalite (creating sand burn-on) and when FeO wets the sand grains, it increases wet ability of liquid steel, making a way for metal penetration. Presence of Argon in mould pores plays an important role in combating these defects because it retards these reactions being an inert gas.

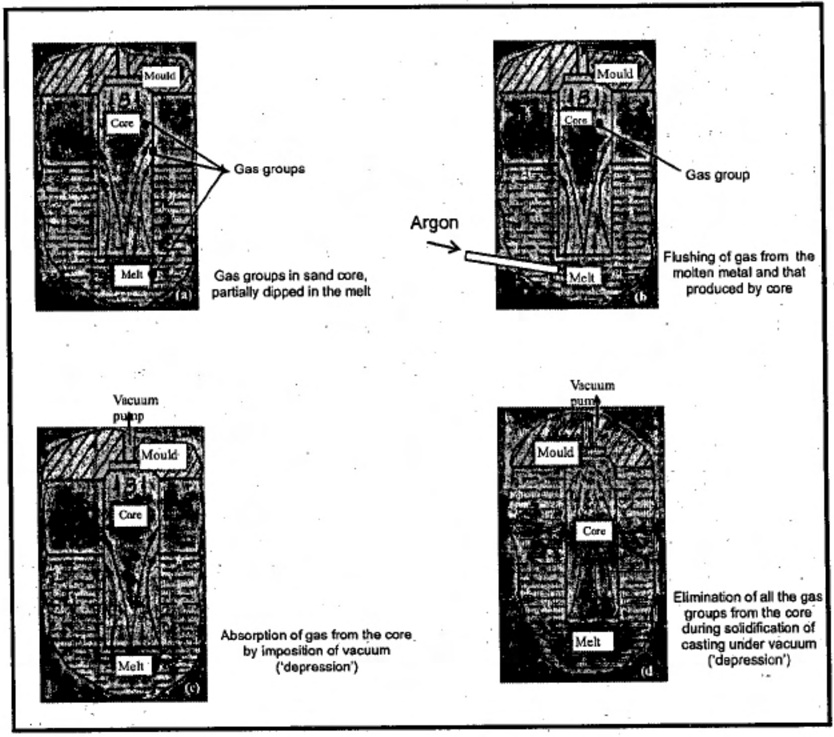

Fig. 10 Schematic illustrating the gas groups in the core and steps for their elimination by applying the casting strategy put forth (a) gas groups present in a sand core, based on some bonding material (b) flushing of gas evolved from the core and ejected to the mould cavity and that dissolved in the molten metal, by introducing argon at an adequate pressure (c) absorption of gas generated in the core by imposition of vacuum (d) Elimination of all the gas groups from the core during solidification of casting under vacuum ('depression').

Like sand moulds, the gas groups are also found in the cores [2, 12]. Fig.10 is a schematic illustrating the gas groups in the core and steps for their elimination by applying the casting strategy put forth (a) gas groups present in a sand core, based on some bonding material (b) flushing of gas evolved from the core and ejected to the mould cavity and that dissolved in the molten metal, by introducing argon at an adequate pressure (c) absorption of gas generated in the core by imposition of vacuum (d) Elimination of all the gas groups from the core during solidification of casting under vacuum ('depression').

5. CONCLUSION

Porosity in castings is due to bubbles being trapped in casting during solidification. Porosity sources include entrapped air during filling, centerline shrinkage that occurs during the final solidification, gases coming from unvented cores, additives added in the moulding material, reactions at the metal mould interface, gases dissolved during melting & casting and inclusions containing gases in their folds [11, 14]. Porosity related defects come about due to the interplay of several phenomena that occur during solidification:

As the melt cools, the solubility of gases dissolved in the melt decreases. If the solubility limit is reached, gas will precipitate out of the melt. If porosity precipitates early in solidification, it can form as spherical bubbles (i.e., gas porosity). If pores precipitate later in solidification, they are constrained by the existing dendritic network and appear in irregular shape. (Carlson K.D., Lin Z et al., 2002). In addition, gases are much less soluble in solid than in liquid, and hence gas is rejected from the solid to the liquid during solidification, which increases gas levels in the remaining liquid. Finally, the pressure gradients associated with metal flowing through the mushy zone to feed solidification shrinkage decreases the pressure in the casting, which further lowers the solubility. So even in the absence of dissolved gases, pores can form solely due to shrinkage. The researches on physic-chemical mechanism of formation of gas porosity and its elimination by the casting technique put forth in the present researches have led to following precise conclusion that two interdependent measures, flushing the gas dissolved in the melt and that collected in the mould cavity, by super imposition with argon and absorption of gas produced within the mould by imposition of vacuum at the mould, can be applied for eliminating both, exogenous and indigenous gas porosity, within the mould cavity.

a) **In moulds**

During casting, three gas groups are present in a sand mould made with some bonding material i.e. melt, part of the mould cavity which is not filled and the sand mould itself. Flushing of gas evolved in the mould cavity and that dissolved in the molten metal by introducing Argon at an adequate pressure.

Absorption of gas generated in the mould by imposition of vacuum in double lined flask. Imposition of vacuum during solidification of casting, resulting in total elimination of all the gas groups.

b) **In cores**

Like sand mould, three gas groups are found in a sand core, made from some bonding material, dipped partially or fully in the melt: the **melt**, gas evolved from the core and ejected to the **mould cavity** and the **core** itself. Flushing of gas evolved from the core and ejected to the mould cavity and that dissolved in the molten metal, by introducing argon, at an adequate pressure. This avoids the gas groups of the molten metal and of mould cavity. Absorption of gas generated in the core by imposition of vacuum. This eliminates the gas present in the core. Elimination of all the gas groups from the core during complete solidification of casting by imposing vacuum ('depression')

The casting techniques put forth, in the form of flushing the gas from the mould cavity & melt and from the mould by imposition of vacuum, is simple and very effective and has been practically applied to avoid both indigenous and exogenous porosity and produce quality castings in small, medium and large ferrous and non-ferrous foundries.

Acknowledgement:

Author is grateful to the foundry men and incharge of the Loco Foundry of Pakistan Railway, Lahore, for granting permission to conduct the casting experiments. In the same token author is grateful to the C.E.O of Marriala Consultants, Engineering and software solutions, Lahore, Pakistan for carrying out the simulation of the casting.

Future Research:

This casting technique may be researched for combating the other defects appearing during solidification. Author is studying this phenomenon and has calculated thermal conductivities of gas mixtures from different sand moulds. The thermal conductivities of gas mixtures from greensand mould and moulds with phenolic urethane, bakelite and sulphatic layee are approximately 3.5 to 4.5 times greater than air, at room temperature and above (upto 500°C), while thermal conductivity of air is 1.35 to 1.5 times greater than Argon. Thermal conductivity of gas mixture from greensand mould is approximately 1.5 times greater than Argon and thermal conductivities of gas mixture from the other three moulds are 5 to 6.5 times greater than Argon at room temperature and above (upto 500°C). It points out that Argon is a worst conductor of heat as compared to air and mould gas mixtures taken from different sand moulds (thermal conductivities: Ar < air < mould gas mixtures). Presence of Argon instead of air and mould gas mixture in the air gap and pores of mould reduces the heat transfer from metal-mould interface to the mould and from mould to the atmosphere. As sand mould retains heat, it offers a steep thermal gradient. The role of this phenomenon in discouraging the appearance of defects in castings may be further studied. Using another casting technique, Saleem et al. (2012) introduced Helium in the sand mould and found that the convection induced by Helium gas reduces SDAS. Small SDAS imparts better tensile properties. Small grain size results in less tendency of hot tears [S. A. Argyropontos (2008), X Wan, R. D. Pehlke (2004), Dontre D (1998)].

REFERENCES

1. http://www.drpervaiz-h.org/Books/miracle%20imposing.pdf
2. http://www.drpervaiz-h.org/Books/morphology.pdf
3. K. Chattopadhay, M. Isac and R. I. L. Guthrie, ISIJ International, 51 (2011) 573.
4. A. A. Burbelko, W. Kapturkiewicz, D. Gurgul and P. Strek, Modeling of the dendrite arms behavior during solidification, Archives of Foundry Engineering, ISS (1897-3310), 9 (2009) 13.
5. D. C. Kent and B. Christoph, Metallurgical and Mat. Transactions, 40A (2009) 163.
6. A. Xingang, B. Yanping, W. Huajie and M. Xin, Special Steel., 2 (2009).
7. S. D. Kumar, Ironmaking & Steelmaking, 36 (6) (2009) 470.
8. M. M. Pariona, G. A. Salem, F. Bertille and N. Cheung, Rev. Latin. De Metall. y Mater., 28 (2) (2008).
9. J. Orlenius and C. T. Hogskola, Factors related to the formation of gas porosity in grey cast iron: Investigation of core gas evolution and gas concentrations in molten iron, Chalmers Publication Library, (2008).
10. K. Akihiko and K. Yasunori, IHI Engineering Review, 40 (2) (2007) 83.
11. Z. Konopka, M. Lagiewka and A. Zyska, Archives of Foundry Engineering, 7 (4) (2007) 101.
12. P. Scarber Jr. and C. E. Bates, Simulation of core gas production during mould fill, American Foundry Society, (2006).
13. H. C. Sun, L. S. Chao, J. of Heat Transfer, 129 (4) (2006) 595.
14. R. Monroe, Porosity in Castings, American Foundry Society, Silver Anniversary Paper, (2005).
15. J. P. Rogler, Modeling of inclusion removal in a tundish by gas bubbling, Ph.D. Thesis, Ryerson University, Toronto, (2004).
16. J. P. Rogler, L. J. Heaslip and M. Mehrvar, Canadian Metallurgical Quarterly, 43 (3) (2004) 407.
17. A. S. Sabau, JOM, 56 (3) (2004) 54.
18. C. M. Fan, R. J. Shie and W. S. Hwang, Ironmaking & steelmaking, 30 (5) (2003) 341.

19. R. L. Naro, Porosity in Iron castings from mould metal interface reactions, Modern Casting, The Free Library (2000).
20. I. Hamill and T. Lucas, Computational fluid dynamics modeling of tundishes and continuous casting moulds, Proceedings of TMS Annual Meeting on Fluid flow phenomena in metals processing, San Diego, USA, (1999) 279.
21. J. Mancini, La Revue de metallurgie CIT, 89 (3) (1992) 269.
22. S. Joo and R. I. L. Guthrie, Canadian Metallurgical Quarterly, 30 (4) (1991) 261.
23. P. Habibullah, Prevention of endogenous blowholes by a new deoxidizing agent, Mehran Univ. Res. J. of Engg. & Tech., 7 (3) (1988) 1.
24. P. Habibullah, A contribution to physico-chemical mechanism of blowhole formation in steel casting by steel mould interaction, Ph.D thesis, UP Bucharest, Romania, (1985).
25. S. C. Sexena, High Temp. Sci., 3 (1971) 168.
26. http://drpervaiz-h.org/Books/puuring.pdf
27. L. Wang, H. G. Lee and P. Hayes, ISIJ International, 36 (1996) 17.